Double-Nanohole Optical Trapping: Fabrication and Experimental Methods

by

Adarsh Lalitha Ravindranath

B.Tech., Amrita Vishwa Vidyapeetham, 2012

A Thesis Submitted in Partial Fulfillment of the

Requirements for the Degree of

MASTER OF APPLIED SCIENCE

in the Department of Electrical and Computer Engineering

University of Victoria

Supervisory Committee

Double-Nanohole Optical Trapping: Fabrication and Experimental Methods

by

Adarsh Lalitha Ravindranath

B.Tech., Amrita Vishwa Vidyapeetham, 2012

Supervisory Committee

Dr. Reuven Gordon, Department of Electrical and Computer Engineering

Supervisor

Dr. Tao Lu, Department of Electrical and Computer Engineering

Academic Unit Member

Abstract

Supervisory Committee

Dr. Reuven Gordon, Department of Electrical and Computer Engineering

Supervisor

Dr. Tao Lu, Department of Electrical and Computer Engineering

Academic Unit Member

Arthur Ashkin's Nobel Prize-winning single-beam gradient force optical tweezers have revolutionized research in many fields of science. The invention has enabled various atomic and single molecular studies, proving to be an essential tool for observing and understanding nature at the nanoscale. This thesis showcases the uniqueness of single-beam gradient force traps and the advances necessary to overcome the limitations inherent in conventional techniques of optical trapping. With decreasing particle sizes, the power required for a stable trap increases and could potentially damage a particle. This is a significant limitation for studying biomolecules using conventional optical traps. Plasmonic nanoaperture optical trapping using double-nanohole apertures is introduced as a solution to overcoming these limitations. Achievements in double-nanohole optical trapping made possible by the pioneering work of Gordon et al. are highlighted as well.

This thesis focuses on the advances in nanoaperture fabrication methods and improvements to experimental techniques adopted in single molecular optical trapping studies. The technique of colloidal lithography is discussed as a cost-effective high-throughput alternative method for nanofabrication. The limitation in using this technique for producing double-nanohole apertures with feature sizes essential for optical trapping is analyzed. Improvements to enable tuning of aperture diameter and cusp separation is one of the main achievements of the work detailed in this thesis.

Furthermore, the thesis explains the modified fabrication process tailor-made for designing double-nanohole apertures optimized for optical trapping. Transmission characterization of various apertures fabricated using colloidal lithography is carried out experimentally and estimated by computational electrodynamics simulations using the finite-difference time-domain (FDTD) method. Optical trapping with double-nanohole apertures fabricated using colloidal lithography is demonstrated with distinct results revealing trapping of a single polystyrene molecule, a rubisco enzyme and a bovine serum albumin (BSA) protein.

Table of Contents

List of Tables

List of Figures

Acknowledgements

"If I have seen further it is by standing on the shoulders of giants."

Sir Issac Newton (1643–1727)

I express my deepest gratitude to all the great women and men who have helped me see further.

A special thank you to **my supervisor, Professor Reuven Gordon,** for giving me the opportunity to work in the frontiers of plasmonics research and for his invaluable guidance during my academic journey.

I would also like to thank **the members of the Nanoplasmonics Research Lab past and present** for their inspiring resilience and kindness, enabling others to achieve success. My gratitude also goes out to **the CAMTEC faculty and staff** for their support.

Above all, I would like to thank **my family and friends** for their unconditional love, support and encouragement.

Dedication

To my family and friends...

Glossary

Common Abbreviations

Abbreviation	Meaning
ALD	atomic layer deposition
AMF	advanced microscopy facility
APD	avalanche photodiode
ARCL	angle-resolved colloidal lithography
BSA	bovine serum albumin
CCD	charge-coupled device
DAQ	data acquistion
DC	direct-current
DNA	deoxyribonucleic acid
EBL	electron beam lithography
FDTD	finite-difference time-domain
FFT	fast Fourier transform
FIB	focused ion beam
GUI	graphical user interface
HCP	hexagonal closed-packed
HWP	half-wave plate
LP	linear polarizer
LSP	localized surface plasmon
NSL	nanoshpere lithography
OEM	original equipment manufacturer
PML	perfectly matched layer
PS	polystyrene
RMS	root mean square
SEM	scanning electron microscope
SERS	surface-enhacned Raman scattering
SIBA	self-induced back-action
SPL	scanning proble lithography
TFSF	total-field scattered-field
w/v	weight-per-volume

Chapter 1

Introduction

The interaction between light, as a form of electromagnetic radiation, and matter appear to elude the classical framework of momentum conservation. The interaction manifests as a system with incident radiation exerting pressure on the object. Johannes Kepler intuitively suggested the concept of radiation pressure from his observations on comets, the direction of their tails always pointing away from the sun. It was a few centuries later that James Clerk Maxwell asserted the hypothesis of radiation pressure in his work unifying electricity and magnetism. Subsequently, the phenomenon was proven experimentally and demonstrated by Pyotr Lebedev in 1901 and Ernest Fox Nichols and Gordon Ferrie Hull in 1903 [2, 3]. At the tail-end of the twentieth century, the invention of lasers made it possible to harness intense radiation pressure. It was then that the potential of radiation pressure came to be realized, leading to the invention of the first-ever single beam gradient force optical tweezers

system [4].

This Chapter delves into the working of a single-beam optical tweezers system and the limitations in trapping using a conventional setup. The Chapter also introduces the self-induced back-action (SIBA) double-nanohole plasmonic aperture as a means of overcoming the limitations of a single-beam optical tweezers setup. The Chapter concludes with an overview and organization of the thesis.

1.1 Single-Beam Gradient Force Optical Tweezers

Pioneering work by Arthur Ashkin, at Bell Labs, in the 1970s and 80s paved the way for the field of optical trapping to emerge with the invention of the first-ever single-beam gradient force optical tweezers system. His invention enabled the manipulation and characterization of single atoms [5] and molecules. Ashkin received well-deserved acclaim in 2018 when the Nobel Prize in Physics was awarded to him for the ground-breaking invention of optical tweezers and their application in biological systems.

Preliminary research by Ashkin focused on the acceleration of a micron-sized latex sphere from radiation pressure [6]. This was followed by the demonstration of levitation of transparent glass spheres [7]. These experiments laid the foundation for the invention of the single-beam gradient force optical tweezers that have been widely

used ever since. After its creation, the setup was simultaneously utilized in experiments to confine neutral sodium atoms [8, 9, 10] and to trap dielectric particles [4].

Within a year after the invention of the tweezers, the first application in biology was demonstrated by the optical trapping and manipulation of viruses and bacteria [11]. The transformative decade in the field of optical trapping culminated with the demonstration of intracellular manipulation and surgery [12], unveiling new frontiers in biomedical research.

1.1.1 Radiation Forces in a Single-Beam Optical Trap

A highly focused electromagnetic radiation with a Gaussian intensity profile, incident on a particle, gives rise to two kinds of forces. These forces enable stable trapping and manipulation of particles in a conventional optical tweezers setup. A perturbative framework, where a particle's influence on the ambient electromagnetic field is negligible, is considered in order to analyze these forces.

Each photon in incident radiation carries with it a momentum that varies inversely to its wavelength. The magnitude of this momentum is expressed as;

$$\| \vec{P} \| = \frac{h}{\lambda}, \tag{1.1}$$

where, h is the Planck's constant and λ is the wavelength of the incident radiation. During scattering, the transfer of momentum between photons and the particle occurs in the direction of propagation of the incident radiation. Of the two forces, the force arising from photons exerting a radiation pressure on the particle is named the scattering force. The other force, the gradient force, is born out of the axial intensity gradient of the incident radiation and is at the core of single-beam optical tweezers systems. It is responsible for opposing the radial displacement of the particle and ensures a stable trap.

In the case of particles in the Mie regime, where the size of a particle is either comparable to or larger than the wavelength of the incident electromagnetic radiation, the forces can be explained with the help of ray optics. Figure 1.1 depicts a high refractive index particle in the waist of an immensely focused Gaussian beam, off the center of the maximum intensity. Neglecting surface reflections, almost all of the rays are refracted through the particle. Consider two rays a and b that upon scattering exert forces $\vec{F}_a$ and $\vec{F}_b$ on the particle in directions ensuring the conservation of momentum. Since ray a has a higher intensity than ray b, the magnitude of force $\vec{F}_a$ will be greater than the magnitude of force $\vec{F}_b$ i.e., $\parallel \vec{F}_a \parallel > \parallel \vec{F}_b \parallel$. The resultant of all the forces from every ray incident on the particle can be resolved into two components: the scattering force, $\vec{F}_{scat}$, acting in the direction of the incident beam and the gradient force, $\vec{F}_{grad}$, arising from the intensity gradient of the beam

and directed towards the center, the highest intensity region of the beam.

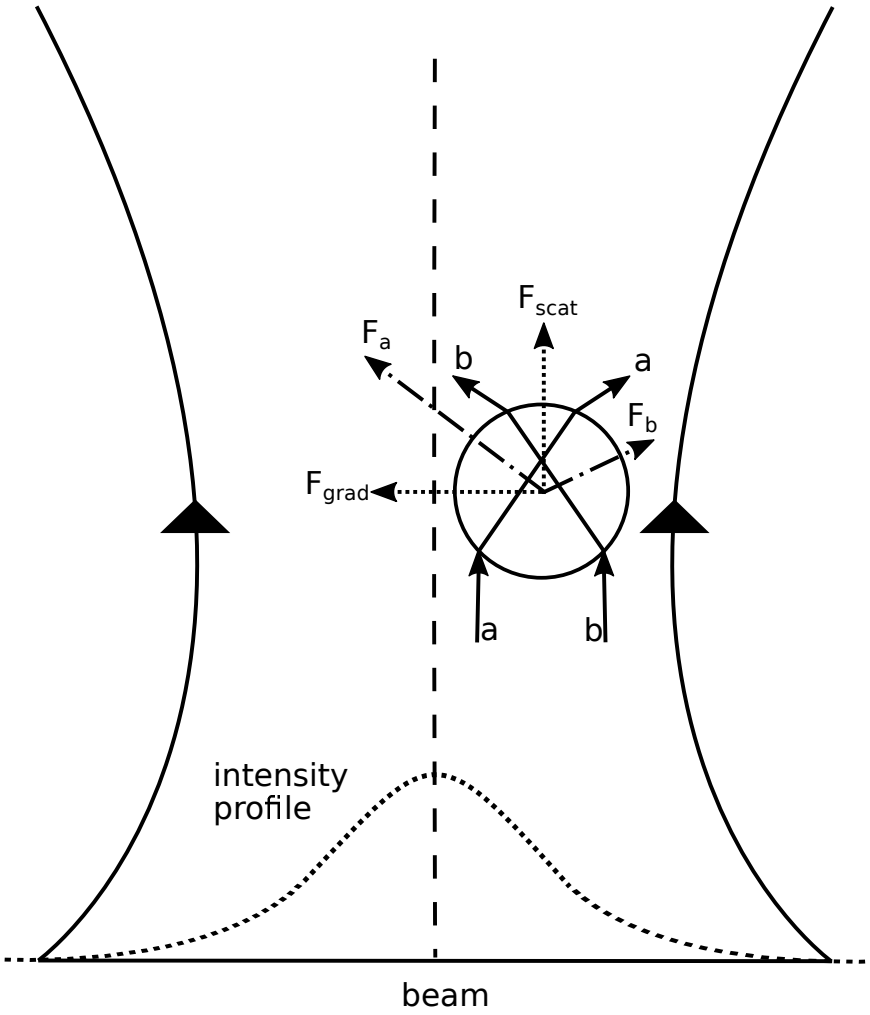

Figure 1.1: Radiation forces acting on a high refractive index particle in an optical trap.

The radiation forces acting on particles in the Rayleigh regime, where the size of a particle is much smaller than the wavelength of the incident electromagnetic radiation,

are analogous to the forces experienced by particles in the Mie regime. The scattering force arises from the dipole moment of the particle and acts in the direction of the incident radiation. It scales directly as the ratio of the sixth power of the particle's size to the fourth power of the wavelength [4]. This is represented in the equation 1.2 below;

$$\parallel \vec{F}_{\text{scat}} \parallel \propto \frac{r^6}{\lambda^4}. \tag{1.2}$$

Here, r is the radius of the particle and λ is the wavelength of the incident electromagnetic radiation.

The gradient force acting on a particle in the Rayleigh regime depends on its polarizability as well as the gradient of the electromagnetic field intensity. It scales as the third power of the particle's size as shown in the equation 1.3 below;

$$\parallel \vec{F}_{\text{grad}} \parallel \propto r^3. \tag{1.3}$$

1.1.2 Limitations of a Single-Beam Gradient Force Optical Trap

Single-beam gradient force optical tweezers have had an impact on many branches in science. However, there are inherent limitations in using the conventional gradient force traps, especially as particle sizes get to the lower end of the Rayleigh regime. These limitations become even more pronounced in the case of biomolecules.

To stably trap a particle in a homogeneous fluid environment, using the single-beam gradient force optical trap, requires overcoming thermally induced Brownian motion and Stoke's drag. The optical power required to oppose Brownian motion scales inversely with the fourth power of the particle's size [4], whereas, the viscous drag experienced by the particle varies linearly with size. The gradient force acting on a particle in the single-beam trap becomes more pronounced than the scattering force with decreasing particle size. However, it only scales as the third power of the size of the particle.

When the particle to be trapped is a biomolecule, almost two orders of magnitude smaller than Abbe's diffraction limit, the optical power required for trapping is significantly greater and potentially above the damage threshold of the molecule. To be

able to effectively trap such biomolecules, well beyond the limits of optical resolution, it is necessary to look beyond the perturbative framework. In the proposed scenario, particles must be able to induce a significant change in the electromagnetic field when trapped under low optical intensities.

1.1.3 Plasmonic Nanoaperture Optical Trapping

Electromagnetic radiation incident on a sub-wavelength aperture in a real metal film generates coherent localized electron charge oscillations (localized surface plasmons (LSPs)) that result in a high-intensity field gradient confined within the aperture. A significant field [13] gradient, within a region smaller than the diffraction limit, is optimal for trapping very small particles mitigating the need for increased optical power.

Nanostructures and nanoapertures were proposed [14, 15] to achieve highly focused field gradients to enable optical trapping of particles in the sub-100 nm regime. Structures like the circular [16, 17], bow-tie [18, 19, 20], rectangular [21] and co-axial [22, 23] nanoapertures as well as other nanoantenna designs [24, 25, 26] have been widely explored and used in trapping. One of the first experiments in plasmonic nanoaperture optical trapping made use of circular nanoapertures. Trapping of 200 nm fluorescent latex beads suspended in water was experimentally shown using a 500 nm circular

aperture fabricated using nanosphere lithography (NSL) [16]. A key study by Gordon et al. demonstrated SIBA in optical traps using circular nanoapertures [17]. This study was instrumental in understanding the effectiveness of nanoapertures in optical trapping. In this work, focused ion beam milling was adopted to fabricate a 310 nm circular aperture and utilized for trapping a single 50 nm polystyrene sphere suspended in water.

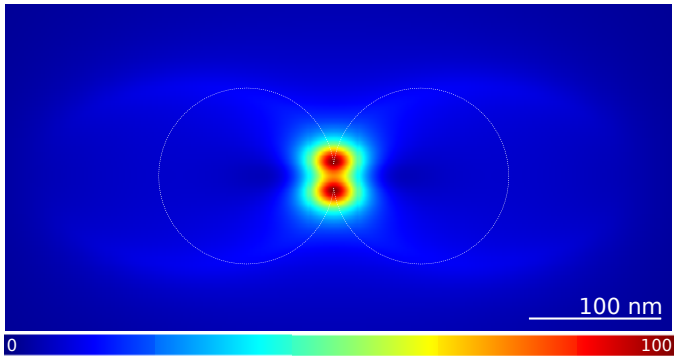

Figure 1.2: FDTD simulation results for electric field intensity distribution in the environment of a double-nanohole aperture excited by electromagnetic radiation polarized along the axis of the cusps for maximum field confinement. The color bar indicates relative field intensities. A contour of the double-nanohole aperture is shown by dotted lines.

Of all the structures that were studied, the double-nanohole aperture emerged as one of the most favourable designs for optical trapping. Following the pioneering work by Gordon et al., an impressive amount of research on the double-nanohole aper-

tures ensued [27], drawing the attention of the scientific community. Beginning with the study of enhanced second-harmonic generation qualities [28] in double-nanohole apertures, subsequent research showed localized field enhancement [29] as well as enhanced transmission [30] capabilities through optimizing the aperture diameter and cusp separation. The structure was utilized successfully in surface-enhanced Raman scattering (SERS) [31] studies as well. One of the main aims of aperture design for optical trapping is to achieve a significant field gradient within a region comparable to the dimensions of the particle, resulting in large optical forces that enable stable trapping. In this regard, the double-nanohole aperture delivers on the desired aperture characteristics.

The potential of double-nanohole apertures in optical trapping was demonstrated with the trapping of 12 nm silica spheres [32]. The dimension of the aperture was chosen according to the size of the particle being trapped. This was one of the first optical trapping experiments using double-nanohole apertures. Subsequently, trapping BSA of size < 5 nm (Stoke's radius) was achieved using the double-nanohole aperture [33, 34]. This was an unprecedented accomplishment, a watershed moment in the history of plasmonic nanoaperture optical trapping. The use of double-nanohole apertures in optical trapping has since had a profound impact on many research efforts in biology. This technique helped in revealing information related to molecular dynamics, like protein-protein interactions, protein-DNA interaction [35, 36], vibra-

tional modes of molecules [37, 38, 39], as well as estimating the molecular weight and sizes [40, 41, 42] of such molecules.

The advantage of a double-nanohole optical tweezer lies in its ability to localize a large field gradient within a region smaller than the diffraction limit around the cusps [43]. Figure 1.2 shows the field distribution at the cusps of a double-nanohole aperture as obtained through FDTD simulation. The details of the simulation design are discussed in Chapter 5.

During optical trapping, the dielectric loading of the nanoaperture by a particle causes a change in the refractive index of the environment surrounding the aperture and makes the aperture optically larger. As a result of Bethe's theory, which states that the optical transmission through a sub-wavelength aperture is proportional to the fourth power of the ratio of the size of the aperture to the wavelength of the incident light [44, 45], a sudden increase in the optical transmission is observed. A very small particle with a size comparable to the cusp separation can immensely change the transmission through the aperture. This makes the double-nanohole extremely sensitive to very small particles, like bio-molecules, creating a conducive environment for trapping.

The double-nanohole has an added advantage of a SIBA on the particle. This en-

hances the ability to maintain a stable trap using optical tweezers. When a trapped particle drifts away from the trap site, a change in the transmission is observed. This generates an equal and opposite force, as per Newton's Third Law, and ensures that the particle is pulled back into the optical trap.

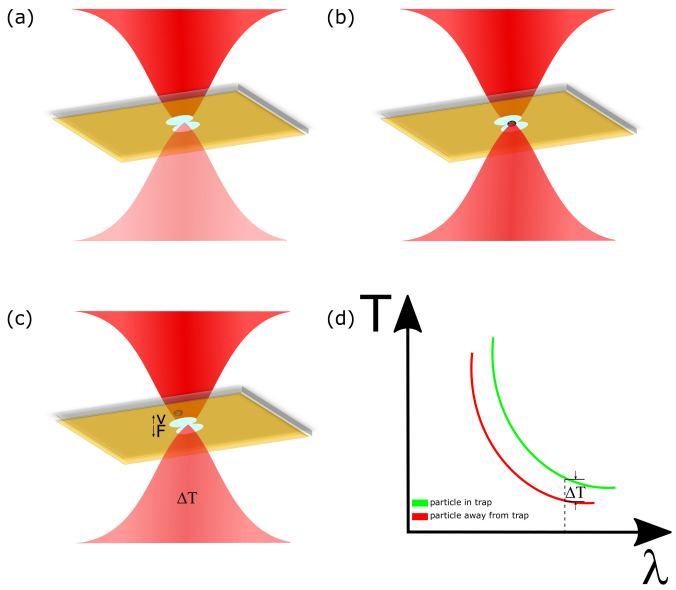

Figure 1.3: Optical transmission in a SIBA double-nanohole trap (a) with no particle trapped, (b) a particle enhancing the transmission by dielectric loading of the aperture when trapped, (c) decrease in transmission (ΔT) as the particle moves away from the trap and (d) a red-shift in the transmission curve observed from the particle's drift.

Figure 1.3 depicts the mechanics of a SIBA double-nanohole optical trap. As a particle enters an illuminated aperture, it becomes optically larger from the dielectric loading and causes an increase in the optical transmission. When the particle moves

away from the aperture, the resulting decrease in transmission induces a momentum change. This, in turn, causes a force to act on the particle inwards, maintaining the trapping. A significant field gradient confinement within the aperture and the SIBA on a trapped particle highlight the effectiveness of using a double-nanohole aperture in overcoming the limitations of conventional single-beam gradient force optical tweezers.

1.2 Fabrication Approaches

In plasmonic nanoaperture optical trapping, fabricating structures with precise dimensions and features is an extremely important step. Therefore, selecting an appropriate fabrication process is crucial. Nanofabrication or fabrication of nanostructures generally adopts one of two broad approaches. One method etches structures from the 'top-down', whereas, the other creates structures from the 'bottom-up'. Depending on the structure being fabricated, each of these methods has its own advantages and disadvantages. Specific structures may require a combination of multiple techniques from each approach to accomplish the desired fabrication.

1.2.1 Top-Down Methods

In top-down methods, the material is etched away to obtain a required structure with smaller dimensions. Photolithography is a fabrication technique that uses optical masks to transfer patterns onto a photosensitive chemical photoresist layer on a substrate. The required structure is obtained by chemical treatment (developing) and etching. Another technique similar to photolithography is the electron beam lithography (EBL). This technique uses a focused electron beam to modify the chemical solubility of an electron-sensitive resist in the desired pattern. The structure is then developed using selective chemical treatment.

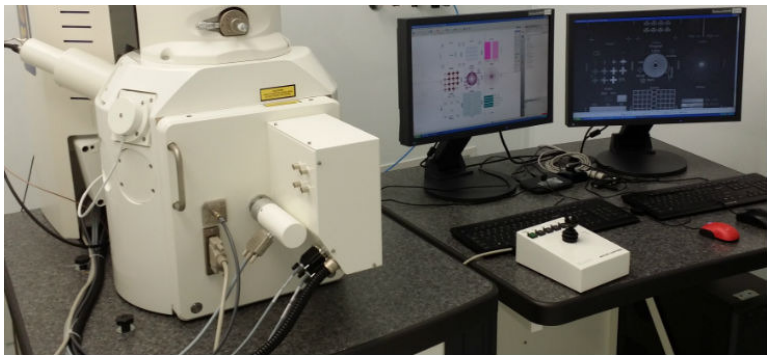

Figure 1.4: AlphRaith 50 EBL system.

The focused ion beam (FIB) milling technique is a top-down approach (discussed in more detail in Chapter 2). This technique uses highly accelerated metal ions,

like low-temperature gallium, to sputter material off the surface and mill structures with precise dimensions. The resolution of focused ion beam systems combined with its ability to etch materials like gold made it one of the most common approaches adopted for fabricating nanostuctures [46]. An alternative technique for fabricating nanostructures makes use of the FIB milling to create a template that can be reused. This technique is the template stripping technique and offers an alternative method for fabricating apertures [47, 48].

Photolithography is a top-down method that has been widely used in fabrication but is not suitable when the feature sizes required are below the diffraction-limited resolution. This is where the EBL technique has the advantage of enabling the fabrication of nanometer-scale dimensions reliably. The downside of using EBL is the high cost per fabrication and low throughput.

1.2.2 Bottom-Up Methods

The bottom-up approach makes use of atoms or molecules as building blocks to create structures layer by layer. The ordering of particles on the surface of a substrate is either allowed naturally or precisely controlled to achieve required shapes or structures. Nanofabrication using bottom-up approaches are generally more cost-effective and reliable, yielding a high-throughput in contrast to resource-intensive and expen-

sive top-down methods. Direct methods like physical or chemical vapour deposition are widely deployed in various bottom-up techniques. More complex serial techniques, like scanning probe lithography (SPL) or atomic layer deposition (ALD), can also be adopted if warranted.

Another widely used technique is the process of natural lithography. Conventionally, templates or masks are created from the self-ordering of particles and are later utilized in fabricating structures by etching or depositing materials [49]. Colloidal lithography is a technique that largely falls under the purview of the natural lithography bottom-up approach and has been well explored and improved upon over the last few decades. A detailed account of this technique is provided in Chapter 2. The customized colloidal lithography process for fabricating double-nanohole apertures with dimensions optimally tuned for optical trapping is discussed in Chapter 4.

1.3 Contributions of Thesis

This thesis aims to highlight the achievement of single-molecule optical trapping using double-nanohole apertures fabricated by a customized colloidal lithography process. This process enables the tuning of aperture dimensions. The thesis also highlights modifications to the experimental setup for improved measurements. The progress of optical trapping from the first single-beam optical tweezers setup to the plasmonic

aperture assisted configuration has been made possible by advances in fabrication techniques in many areas of science. From optical parts to semi-conductor detectors and lasers, improvements in corresponding fields have enabled the creation of a cost-efficient, high-performance single-beam optical tweezer setup. A holistic improvement to cost, quality, reliability and performance in plasmonic nanoaperture optical trapping has been made possible through refining the technique of fabricating double-nanohole apertures using colloidal lithography. Using this technique, trapping of single-molecules less than 5 nm (Stoke's radius) has been achieved.

This thesis is organized into six chapters. Chapter 1 delves into the history of optical trapping, the theory of operation, the limitations of conventional methods and the solution to overcome these challenges. A brief review of different fabrication approaches is provided with detailed accounts given in subsequent chapters. In Chapter 2, conventional optical tweezers setup and fabrication methods for double-nanohole apertures are discussed. In addition, in Chapter 2, an overview of the colloidal lithography technique is provided. Chapter 3 discusses the improvements to the experimental setup, bettering the quality of measurements made while enabling different types of experiments to be performed. Chapter 4 discusses the central work on colloidal lithography and optical trapping that highlights the contribution of the thesis. Details of the fabrication and experimental procedure, including results from optical trapping experiments presented in this Chapter, are based on the publication by the author [1];

Adarsh Lalitha Ravindranath, Mirali Seyed Shariatdoust, Samuel Mathew, and Reuven Gordon. Colloidal lithography double-nanohole optical trapping of nanoparticles and proteins. Opt. Express, 27(11):16184-16194, May 2019.

Transmission characterization of double-nanohole apertures with different dimensions was carried out experimentally. The apertures were fabricated using 200 nm, 300 nm and 500 nm polystyrene spheres. Experimental results of transmission measurements are presented in Chapter 4. Additionally, FDTD simulations were performed using commercially available software from Lumerical Inc. to validate measurements from experiments. Details of the simulation design and the subsequent results from simulations are discussed in Chapter 5. Chapter 6 summarizes the thesis and provides an outlook on future research efforts using the colloidal lithography double-nanohole optical trapping technique.

Chapter 2

Previous Approaches

Past approaches adopted in optical trapping using double-nanohole apertures are discussed in this Chapter. Details regarding previous experimental setup, its configuration and the process of fabrication using FIB milling are provided. In addition, an account of the history and development of the colloidal lithography technique is given with an emphasis on fabricating nanoapertures like the double-nanohole aperture. Improvements to conventional methods, both in the experimental setup and the fabrication procedure, are discussed in subsequent chapters highlighting the contributions of this thesis.

2.1 Conventional Optical Tweezers Setup

Figure 2.1 shows a schematic of a basic optical trapping setup. Conventionally a commercially available setup from Thorlabs (OTKB) has been used in experiments. The configuration of a basic setup is discussed in this section.

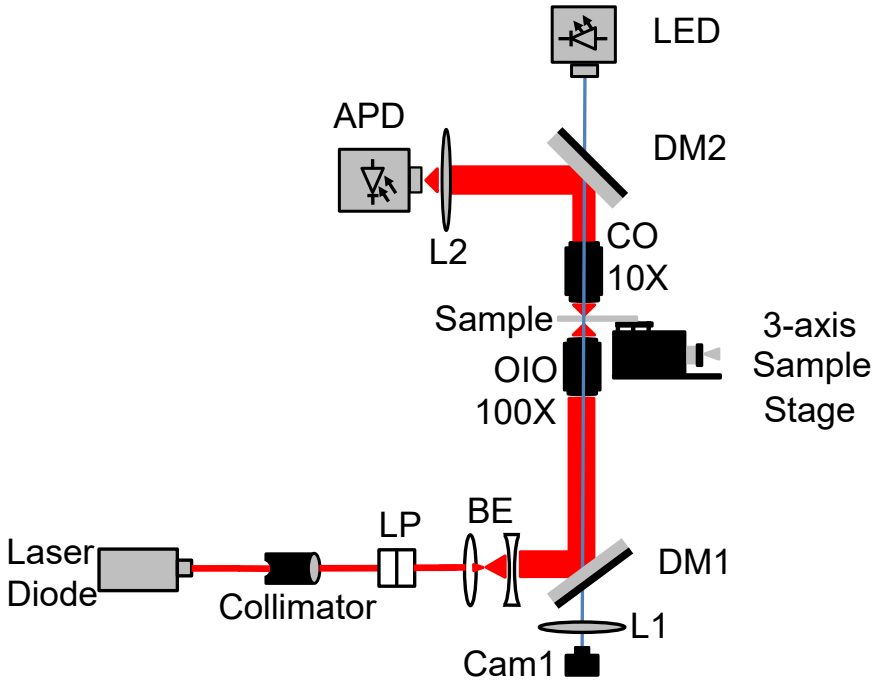

Figure 2.1: Thorlabs modular optical tweezer system. The various components labeled are: linear polarizer (LP), beam expanding (BE) lenses, short-pass dichroic mirror (DM1), focusing lens (L1), oil immersion objective (OIO), collection objective (CO), short-pass dichroic mirror (DM2), focusing lens (L2) and avalanche photodiode (APD).

The system adopts an inverted microscope arrangement of high numerical aperture microscope objectives with confocal alignment. The trapping laser is a fiber-coupled (APC/FC) 14-pin butterfly diode mounted on a laser controller. An appropriate fiber port collimator is used for collimating the beam. The polarization of the beam is limited using a linear polarizer. The back focal plane of the bottom objective is filled by expanding the beam using a Galilean beam expander to allow efficient focusing.

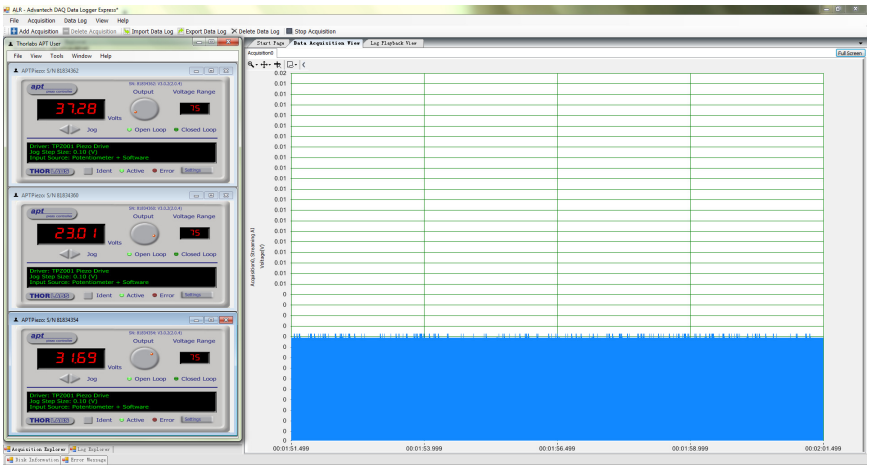

Figure 2.2: Thorlabs APT GUI docked with Advantech DAQNavi DataLogger software environment.

A short-pass dichroic mirror is used to image the sample on a charge-coupled device (CCD) camera. This allows light from the white light source to be transmitted while reflecting the incident laser. A 100× oil immersion microscope objective with 1.25 numerical aperture focuses the expanded laser beam. The width of the focused laser

beam is reduced to around 1.1 μm. A 10$\times$ collection objective with a 0.25 numerical aperture collects the transmission prior to being measured. The setup consists of a 3-axis piezoelectric stage for 20 nm precision translation enabled manually as well as through a graphical user interface (GUI). This is extremely critical for positioning apertures fabricated on a sample directly under the laser and focusing the laser on an aperture by adjusting the z-height. Finally, a silicon-based avalanche photodiode (APD) enables measurement of the collected transmission with an integrated data acquisition (DAQ) system. Figure 2.2 shows the GUI for the 3-axis translation stage along with the DAQ software environment. The software is made available by the original equipment manufacturers (OEMs).

2.2 Focused Ion Beam Milling

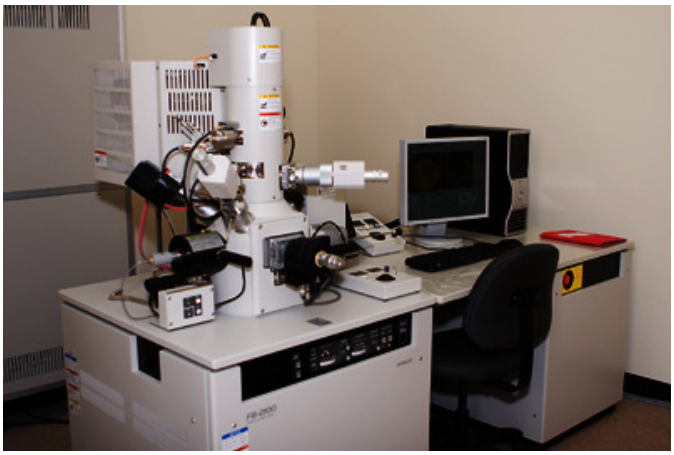

Figure 2.3: Hitachi FB-2100 FIB system.

Most FIB systems, an example shown in Figure 2.3, have many functions including etching, deposition and imaging. For the purpose of nanofabrication through etching, highly accelerated ions from the FIB source sputter material from the surface of a sample. Mostly, a liquid metal ion source like gallium is used. A tungsten needle helps concentrate the flow of the gallium to a tip when heated. An extremely high electric field ionizes the gallium and causes an accelerated emission. The beamwidth is controlled through apertures. Electrostatic lenses are used to control stigmation and focus.

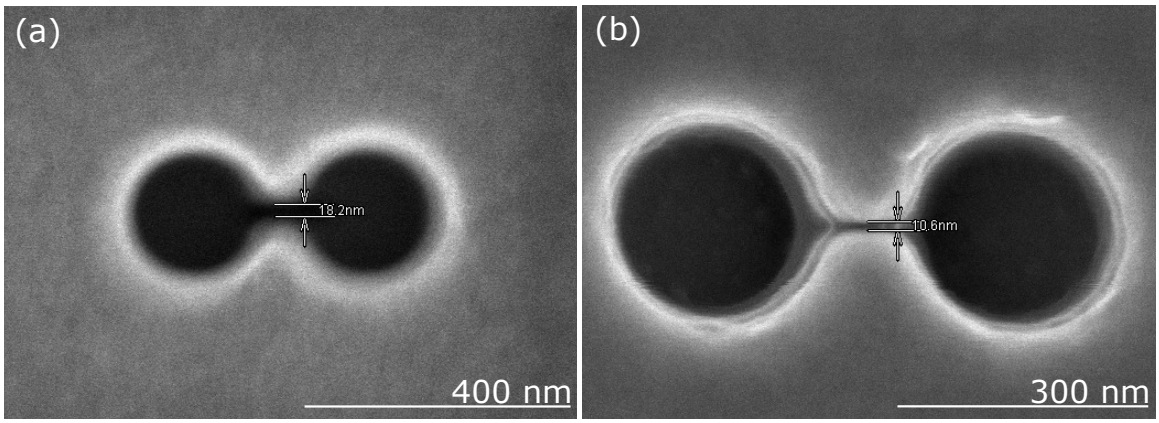

Figure 2.4: Double-nanohole apertures fabricated using the FB-2100 focused ion beam system.

The scanning electron microscope (SEM) images of double-nanohole apertures depicted in Figure 2.4 were fabricated using FIB milling. The Hitachi FB-2100 at the

Advanced Microscopy Facility (AMF) at the University of Victoria was used for the fabrication of these apertures. A commercially available slide from EMF Corp., with a 100 nm gold layer adhered on a glass substrate through a 5 nm titanium adhesion layer, was used for milling these structures. To fabricate the double-nanoholes in Figure 2.4 a focused gallium ion beam with an acceleration voltage of 40 kV and a limiting beam aperture of 5 μm was used to mill the gold at 35 k$\times$ magnification.

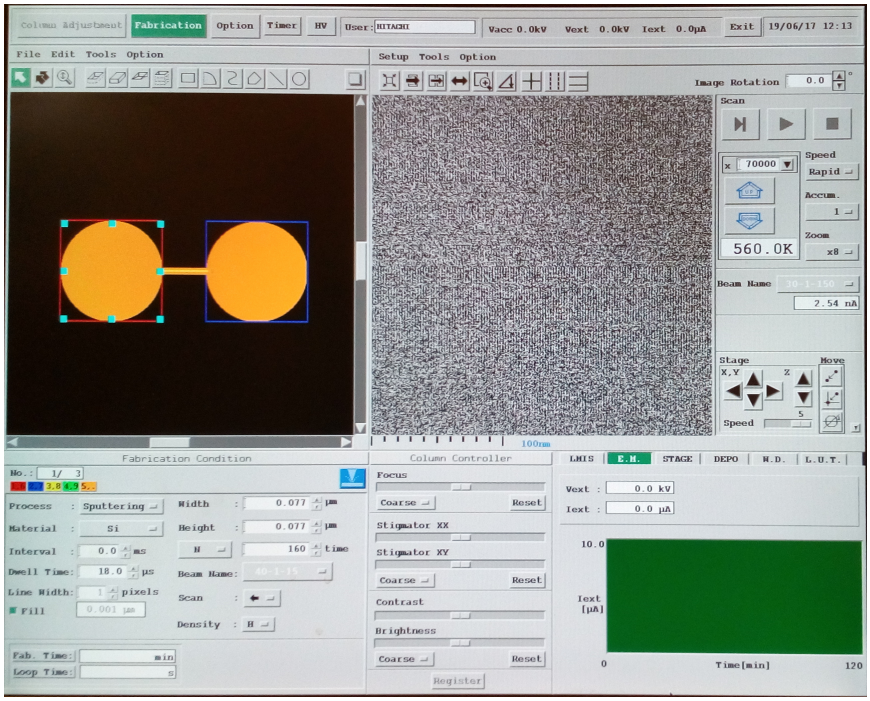

Figure 2.5: GUI on the FB-2100 FIB system.

The milling time (dwell time$\times$number of passes), as well as the distance between the two circular apertures, needs to be optimized to obtain the desired cusp separation.

A dwell time of 8-10 μs, 50-60 passes and a distance between the apertures of 30-40 nm usually works well for a cusp separation < 30 nm. Large fiduciary markers are fabricated around the double-nanohole structures for ease of identification on the optical tweezers setup. Aperture diameters and other parameters mentioned above can be controlled using the FIB GUI (figure 2.5).

2.3 Colloidal Lithography

Lithography, a process invented by Alois Senefelder at end of the eighteenth century for printing and publishing, finds its etymology in the Greek words 'lithos' and 'graphein' that mean 'to write with stone'. This technique of imprinting using a template of sorts has found relevance in micro and nanofabrication. A nanofabrication technique that has been widely researched is the colloidal lithography technique and is discussed in detail in this section.

One of the very first published works that utilized the principles of lithography for nanofabrication enabled sub-100 nm resolution using contact imaging with visible light [50]. This was accomplished by Fischer and Zingsheim in 1981. Their efforts laid the foundation for a nanolithographic technique that was improved upon and popularized as "natural lithography" by Deckman et al. in 1982 [51] and subsequently furthered by Van Duyne et al. as "nanosphere lithography" [52, 53]. The basis of

all these works lie in the use of dispersed colloidal spheres fabricated by conventional emulsion polymerization or sol-gel synthesis techniques. This nanolithographic technique essentially relies on the formation of random or ordered two-dimensional arrays or three-dimensional crystals of colloidal particles on any substrate surface, later used as a mask for etching or deposition. This led to the adoption of the term "colloidal lithography"as an alias for this technique.

The natural self-assembly of monodisperse spheres on substrates can be achieved through various methods like spin coating or drop coating. After the suspension of the colloidal spheres is transferred to a substrate, the particles freely diffuse towards their lowest energy configuration. This is possible with modified surface chemistry and charge repulsion between the surface of a substrate, such as glass, and specific functional groups in the colloidal molecule. During evaporation, capillary forces cause crystallization of the particles forming complex aggregations or randomly organized layer(s) through self-assembly. For achieving an ordered monolayer mask, with a hexagonal close-packed (HCP) pattern on the substrate without templates, using spin coating has been quite successful. Double layers can be created by adjusting the concentration of the suspension used. Once the mask has been fabricated, the etching of the substrate or deposition of metals can be performed depending on the desired structure and specificity of the intended application. Following this step, the mask or the colloidal layers can be peeled off or removed through sonication in a solvent,

revealing the desired structure.

Complex patterns can be fabricated using the colloidal lithography technique [54]. Fabrication of structures with complex features is possible through methods like angle-resolved colloidal lithography (ARCL) by non-zero incident angle deposition in combination with modification of particle dimensions by swelling using an organic solvent or deformation through plasma etching [49, 55]. This is especially useful for fabricating structures with optical characteristics tuned for specific applications.

Optical properties of structures like single-nanohole apertures fabricated using colloidal lithography have been widely researched [56, 57, 58]. The earliest works that used colloidal lithography to fabricate nanohole apertures were carried out by Fischer. These works studied the optical characteristics of circular apertures for use in ultramicroscopy [59] and surface-enhanced spectroscopy [60]. Single nanoholes fabricated using colloidal lithography have also been used in optical trapping [16]. Fabrication of double-nanohole apertures using colloidal lithography has been demonstrated as well, and their non-linear optical properties have been investigated [61]. The smallest cusp separation for double-nanohole apertures reported was in excess of 180 nm. These dimensions would not be effective in trapping sub-Rayleigh particles.

Colloidal lithography, inherently a parallel process with a high-throughput, is ex-

tremely cost-effective but is susceptible to a variety of defects arising from non-uniform diffusion and undesired aggregations as well as from substrate surface imperfections and impurities. Despite these issues, obtaining a defect-free region with the desired mask is still possible. Defect-free masks obtained through methods like template-assisted epitaxy are expected to improve the quality of fabrication, especially as features of structures become more complex. One of the greatest challenges with colloidal lithography has been in obtaining feature sizes in the sub-10 nm regime. Later chapters will show that customizing the colloidal lithography technique with dimension tuning, using appropriate plasma etching, enables the fabrication of structures with feature sizes in the 10 nm regime. This results in plasmonic characteristics favourable for optical trapping of particles < 5 nm (Stoke's radius). Chapter 4, details the colloidal lithography technique used in fabricating double-nanoholes with the tuning of aperture diameter and cusp separation to obtain the optimal structure for trapping.

Chapter 3

Experimental Approaches

Optical tweezers conventionally used for trapping experiments in the past had limitations with respect to the type of measurements possible and the quality of measurements acquired. To effectively perform optical trapping, improvements were made to the existing system to enable additional measurement options and eliminate vulnerabilities with regard to noise that affects data integrity. The optical trapping setup was repurposed, as shown in Figure 3.1. These modifications are detailed in the sections that follow.

3.1 Noise Reduction

Experimentally, the light gathered by the collection objective in the optical trapping setup is detected and converted to a voltage signal by the APD. In the setup used,

the electrical signal is acquired by a USB-4771A DAQ module from Advantech. It is configured to a single-ended 2.5 V (APD limitation) mode prior to the acquisition, using the Advantech DAQNavi Datalogger software. A 100 kHz sampling frequency is chosen to ensure that the transient data is captured during any trapping event.

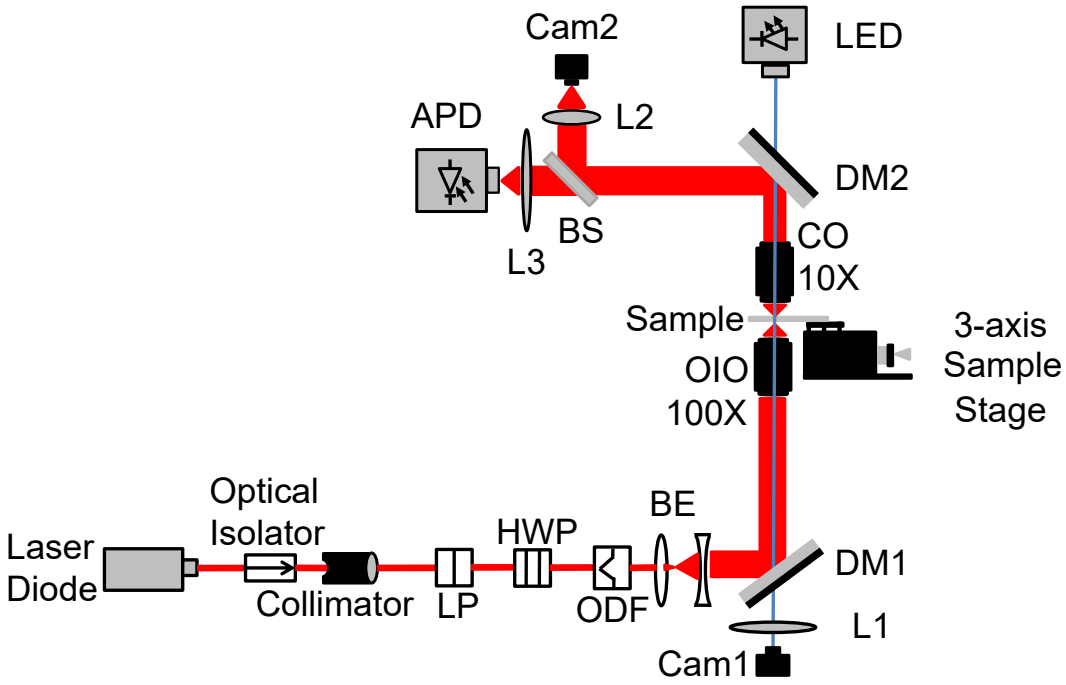

Figure 3.1: Schematic of the modified optical trapping setup [1]. The various components labeled are: linear polarizer (LP), half-wave plate (HWP), optical density filter (ODF), beam expanding (BE) lenses, short-pass dichroic mirror (DM1), focusing lens (L1), oil immersion objective (OIO), collection objective (CO), short-pass dichroic mirror (DM2), beam splitter (BS), focusing lens (L2 and L3) and avalanche photodiode (APD).

The data acquired by the DAQ is prone to corruption by noise. The interfering noise arises from different sources, such as nearby electrical lines, ground loops within the system, optical feedback into the laser source or even structural vibrations in the research facility.

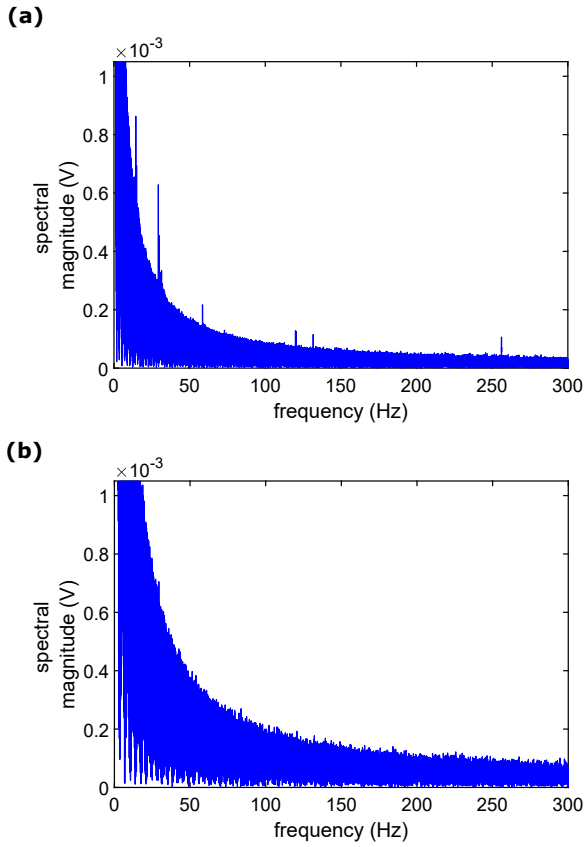

Figure 3.2: Frequency spectrum of acquired data indicating (a) spectral noise components without preventive measures and (b) absence of spectral noise components with measures in place.

Figure 3.2 (a) depicts the various spectral components introduced into the acquired data from noise sources. The plot is a fast Fourier transform (FFT) of the data acquired from the APD. The effect of the electrical line noise can be observed as components of 60 Hz in the plot. These noise elements modulate the trapping signal corrupting the information critical to characterizing the trapping event.

Multiple measures were adopted to address the issue of noise interference. Firstly, the ground loops within the system were eliminated by using isolated grounding mechanisms. A single power plug was used to power all the components through an appropriate extension outlet. Proper shielding of wires, connectors and other exposed components was ensured. A Faraday cage casing, using aluminum foil, for the data acquisition module was put in place to prevent line noise interference during data acquisition. The computer connected to the DAQ and other peripherals were placed on a sturdy shelf.

With regard to noise arising from the laser source, an optical isolator with the appropriate range of operation is recommended. The isolator prevents any reflection from entering back into the laser cavity by redirecting the propagation path of the back-reflected laser. This prevents damage to the laser as well as possible interference. In order to create a stable lasing output, the laser diode controller can be modulated using an external source. An arbitrary function generator with a direct current (DC)

output signal can be used to drive the laser diode controller for extremely stable operation. Finally, the structural vibrations arising in the facility can be mitigated by using an optical bench with a pneumatic shock-absorbing mechanism. Additionally, a benchtop vibration isolation platform, as shown in Figure 3.3, can be used to mount the entire trapping setup.

Figure 3.3: Benchtop vibration isolation platform.

The benefit of adopting precautionary measures is observed in Figure 3.2 (b) FFT plot. Unwanted spectral peaks previously seen are suppressed ($\sim$ 2 dB). This results in an improved quality of measurement during optical trapping.

3.2 Further Modifications

A rotation mount with graduations for fine angle tuning of a half-wave plate (HWP) was incorporated in the setup. This enables the polarization dependence characterization of apertures to be performed with accuracy. The polarization of the laser incident on an aperture can be tuned through precise angles by rotating the HWP when mounted on the rotary mount during measurement.

Furthermore, to observe the scattering of light through apertures, another CCD camera was mounted on the setup. A beam-splitter was used to enable CCD camera monitoring and APD detection at the same time. One of the purposes of using CCDs in both the transmission and reflection modes is to make it possible to analyze trapping events through a frame difference method from different perspectives. In experiments where transmission spectral measurements are required, a spectrometer probe can be mounted in place of the transmission CCD. The modified optical trapping setup configuration has proven to be extremely versatile, enabling a variety of experiments to be performed efficiently and accurately.

Chapter 4

Colloidal Lithography and Optical Trapping

In this Chapter, modifications to the colloidal lithography technique for fabricating double-nanohole apertures are explained. The process to tune the dimensions of the structure are also discussed. Further, the results from the optical trapping of a single polystyrene nanoparticle, a rubisco enzyme and a BSA protein using the fabricated double-nanohole apertures are analyzed.

4.1 Fabrication

Figure 4.1 depicts the process flow for fabricating double-nanohole apertures using the colloidal lithography technique. Firstly, microscope slides of 1 mm thickness are

cut to appropriate dimensions using a glass engraving tool and sonicated in an ethanol bath. The slides serve as the substrate for the samples being fabricated. Once blow-dried with compressed nitrogen, the prepared slides are stored in clean plastic petri dish containers.

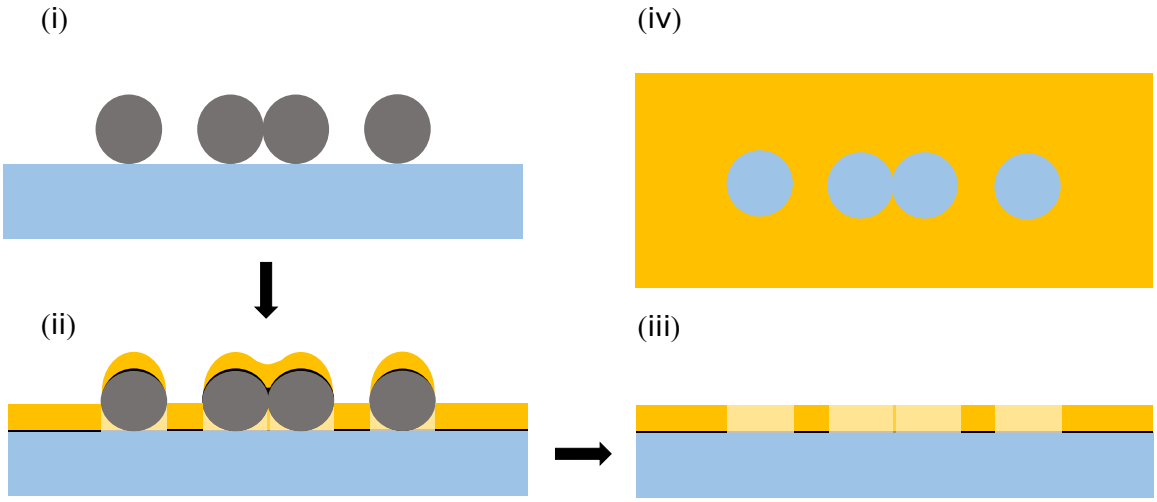

Figure 4.1: Process-flow diagram depicting the various steps in fabricating double-nanohole apertures using colloidal lithography with polystyrene spheres [1]. (i) Drop-coated polystyrene spheres attached to a glass substrate. (ii) Sputter-coated Au-Ti layers on substrate with spheres. (iii) Substrate after sonication in ethanol with desired apertures. (iv) Top-view of the substrate sample showing single and double-nanoholes.

Before commencing the fabrication process, the appropriate diameter of the polystyrene spheres is decided. A commercially available suspension (from Thermo Fisher or

Sigma Aldrich) with the desired sphere diameter is obtained. Next, a 0.01% w/v colloidal suspension in ethanol is prepared. This concentration is found to be optimal for fabricating double-nanoholes with favourable inter-dimer separation. The prepared suspension is then drop-coated on the microscope slides uniformly. A micropipette is used to drop-coat the colloidal solution on the substrate in a line-by-line manner. After drop-coating, the perti dish containers are covered to prevent impurities, like dust, from contaminating the surface. The polystyrene spheres suspended in the solution are then allowed to adhere to the surface of the substrate as the solution dries out.

Figure 4.2: Harrick PDC plasma cleaner used for surface etching.

During evaporation, polystyrene spheres conglomerate into clusters and adhere to the surface of the substrate. The cluster of interest is a dimer that will result in a double-nanohole aperture once the fabrication procedure is complete. To tune the dimensions

of the dimers, and in turn the resulting double-nanohole apertures, the prepared samples are cycled through a plasma etching process. Figure 4.2 shows a plasma cleaner from Harrick used for etching the samples. A sample without undergoing any plasma etching is set aside as baseline control. The other samples being fabricated are placed side-by-side in the plasma cleaner and removed one at a time after specific etch times.

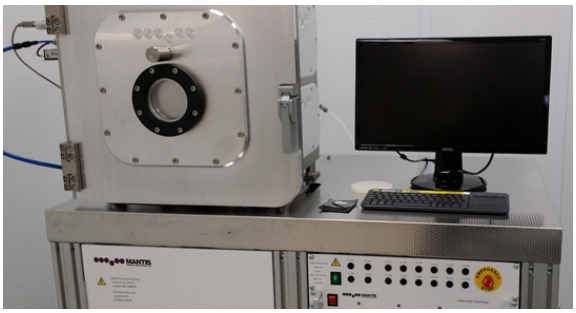

Figure 4.3: Mantis QUBE sputter deposition system.

After the selected slides have undergone plasma etching, sputtering is carried out. Samples prepared for the trapping experiment presented in this thesis were sputtered using the AMF's Mantis QUBE system shown in Figure 4.3. The samples are attached to the sputtering base plate using double-sided Scotch tape. The appropriate targets for sputtering are ensured to be in their respective holders before initiating the process. First, a 5 nm layer of titanium is deposited as an adhesive layer, followed by a 70 nm gold layer. After the sputtering is complete, the samples are removed by dislodging them using the base plate screws and subsequently sonicated in an ethanol

bath for at least 3 minutes to remove the polystyrene beads. Once the beads are removed, the desired apertures are created in the sample. The thickness of the sputtered layers are critical to the success of the fabrication. If the thickness is greater than the radius of the polystyrene spheres adhered to the sample, undesired rips are created upon sonication, rendering the fabrication ineffective.

4.2 Collocation and Characterization

Figure 4.4: Hitachi S-4800 SEM.

To locate the double-nanohole apertures fabricated in a sample, using the optical trapping setup, SEM images of the sample are necessary. Before imaging any sample under the SEM, appropriate fiduciary marker(s) must be inscribed on the sample. SEM images make locating the apertures in the optical trapping setup easier.

Figure 4.5 showcases multiple double-nanoholes obtained from the fabrication through colloidal lithography combined with plasma etching using 200 nm polystyrene spheres. The Hitachi S-4800 at the AMF in the University of Victoria, shown in Figure 4.4, was used for imaging these apertures. The dimensions of the double-nanoholes, aperture diameter and cusp separation, are represented in Figure 4.8 (a) with respective etch times.

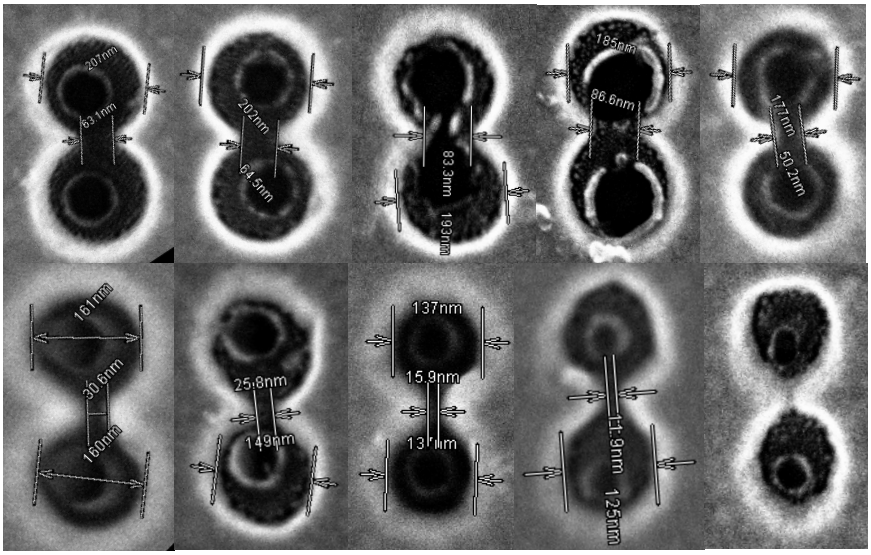

Figure 4.5: SEM image collage of a wide range of double-nanohole aperture dimensions fabricated through colloidal lithography and plasma etching using 200 nm polystyrene spheres [1].

Images of the apertures with respect to the fiduciary mark are required to locate specific apertures for experiments on the optical trapping setup. As shown in Fig-

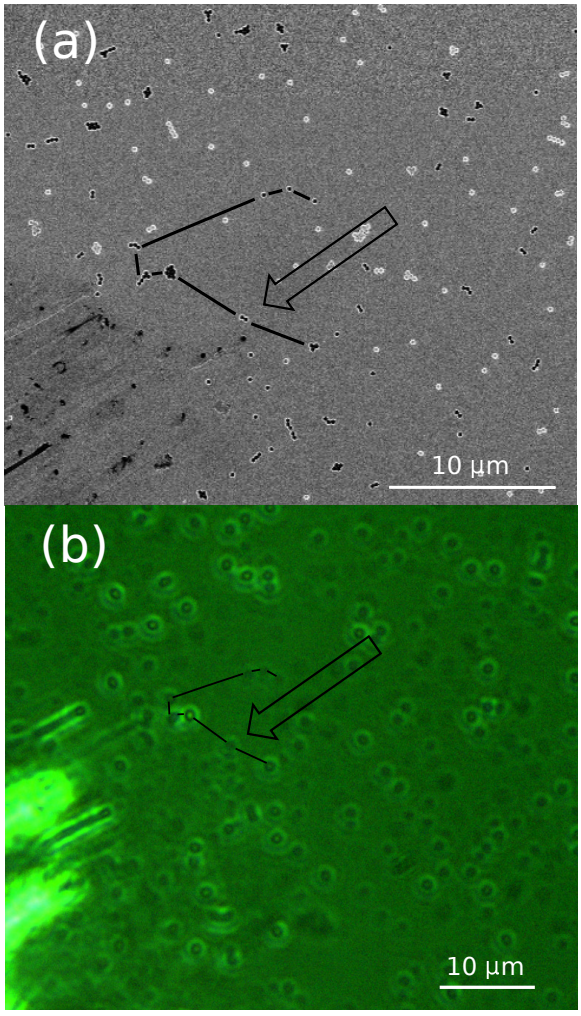

Figure 4.6: Constellation mapping and collocation of a double-nanohole amongst numerous apertures fabricated on a sample with the tip of a fiduciary line in the bottom left corner as seen under (a) SEM and (b) optical trapping setup.

ure 4.6 (a), a unique constellation is identified using the SEM image and mapped to a double-nanohole. Figure 4.6 (b) shows the image of the same sample under the optical trapping setup. Since larger apertures typically appear brighter because of longer wavelength cut-offs, the brighter points observed in the trapping setup image can be mapped to corresponding apertures in the SEM image. The constellation map from the SEM image is collocated on the image from the optical trapping setup to pinpoint the location of the double-nanohole. Identifying a specific double-nanohole amongst numerous apertures can be repeated successfully and reliably through the process of collocation.

A polarization dependence characterization study is performed on a double-nanohole fabricated using the colloidal lithography technique. Figure 4.7 (a) shows a double-nanohole fabricated with 200 nm polystyrene spheres without plasma etching. The cusp separation is approximately 60 nm. Figure 4.7 (b) shows the polar plot of normalized transmission intensities obtained through the double-nanohole with varying angles of polarization of a focused 980 nm laser illuminating the aperture. The values are normalized to the maximum intensity measured by the APD on the optical trapping setup. The transmission varies as a function of the polarization angle of the incident laser. The maximum transmission is measured when the polarization of the incident electromagnetic radiation is aligned with the axis of the cusps (144°). The polarization was tuned between $0° - 360°$, in 4° increments, using a half-wave plate

on a rotation mount. A Malus' law fit is plotted in comparison to the experimentally measured values, and the degree of polarization is calculated to be 0.29.

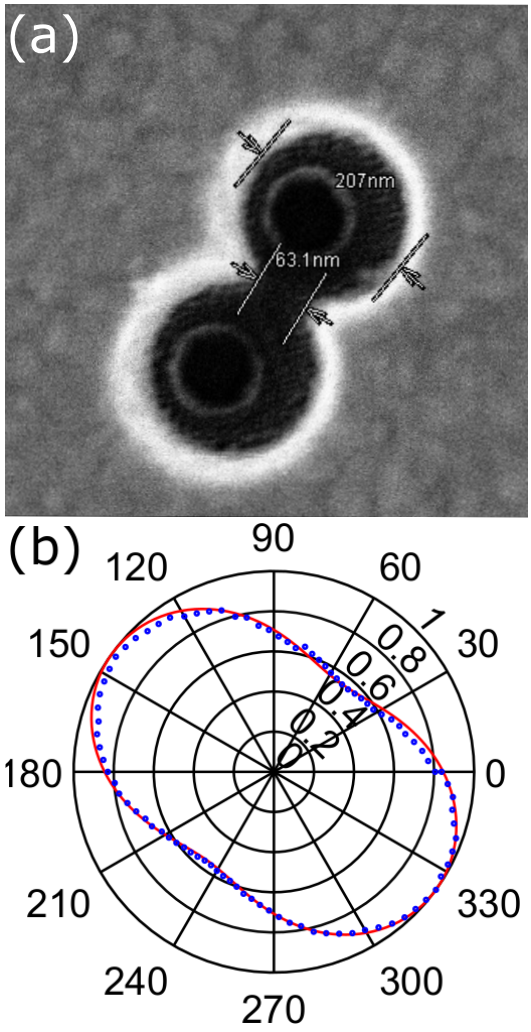

Figure 4.7: (a) SEM image of a double-nanohole aperture. (b) Polarization dependence characterization of the double-nanohole shown in (a). Blue dotted line indicate experimental values. Continuous red line indicates theoretical Malus' law fit.

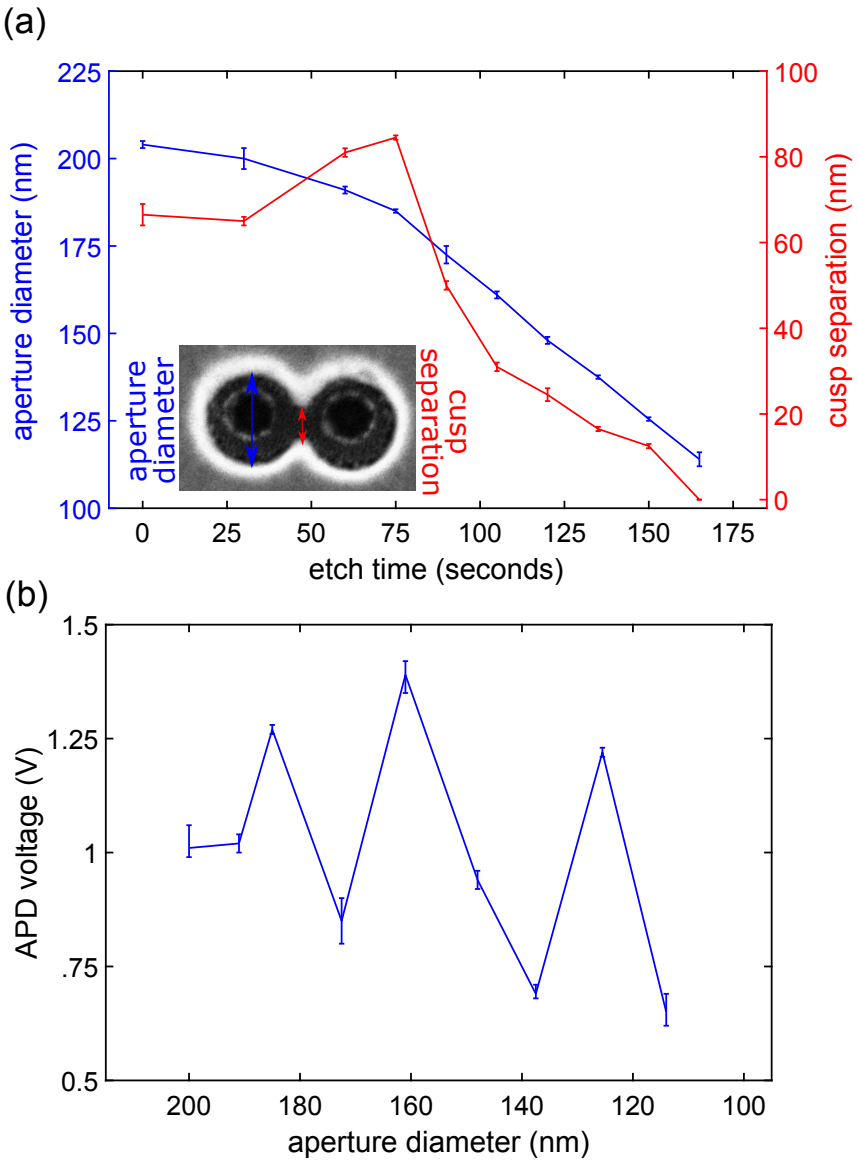

Figure 4.8: (a) Effect of plasma etching on the double-nanohole dimensions fabricated using 200 nm polystyrene spheres. (b) Transmission measurements through apertures fabricated using 200 nm polystyrene spheres [1].

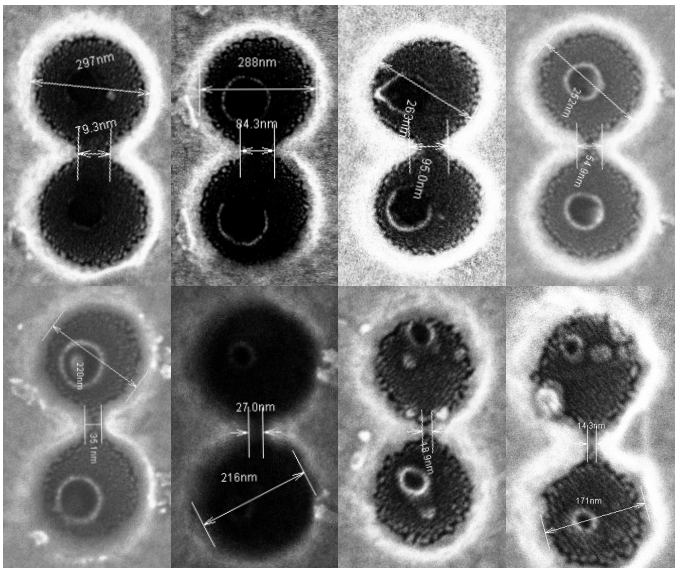

Figure 4.9: SEM image collage of a wide range of double-nanohole aperture dimensions fabricated using 300 nm polystyrene spheres.

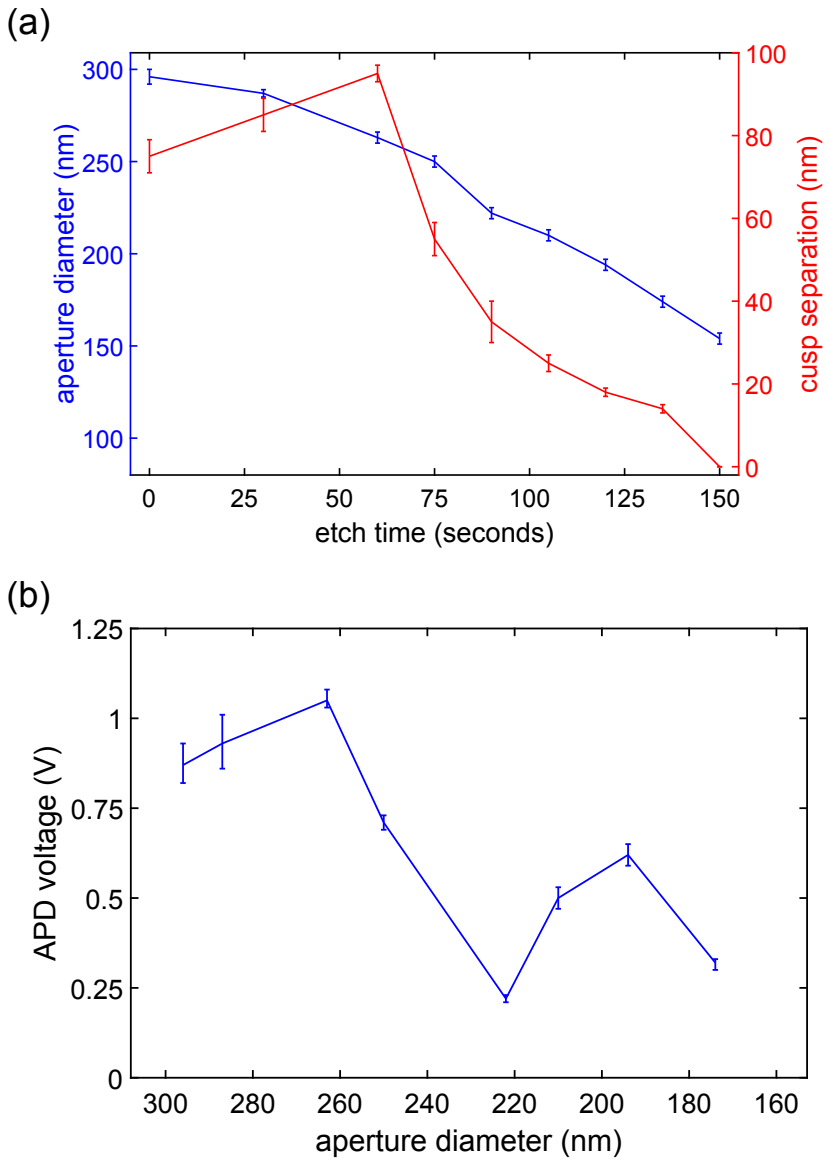

Figure 4.10: (a) Effect of plasma etching on the double-nanohole dimensions fabricated using 300 nm polystyrene spheres. (b) Transmission measurements through apertures fabricated using 300 nm polystyrene spheres [1].

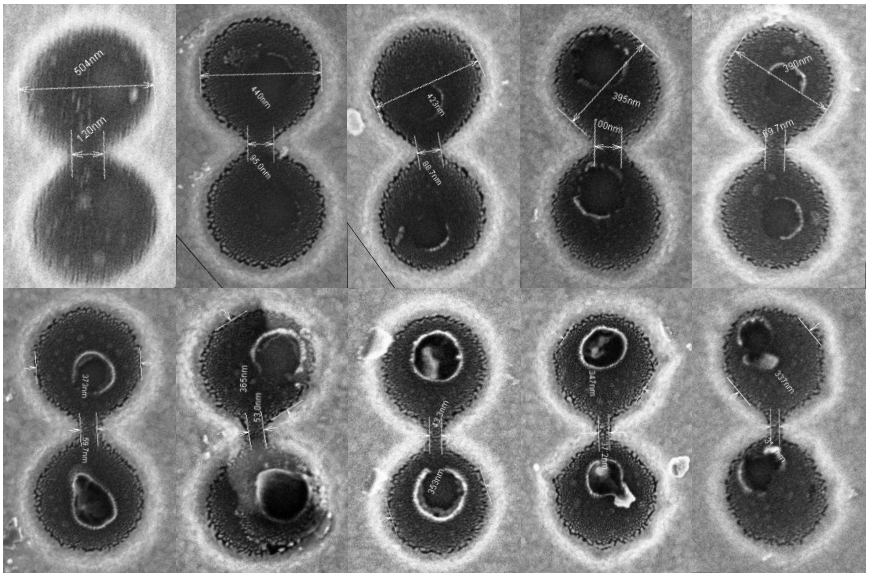

Figure 4.11: SEM image collage of a wide range of double-nanohole aperture dimensions fabricated using 500 nm polystyrene spheres.

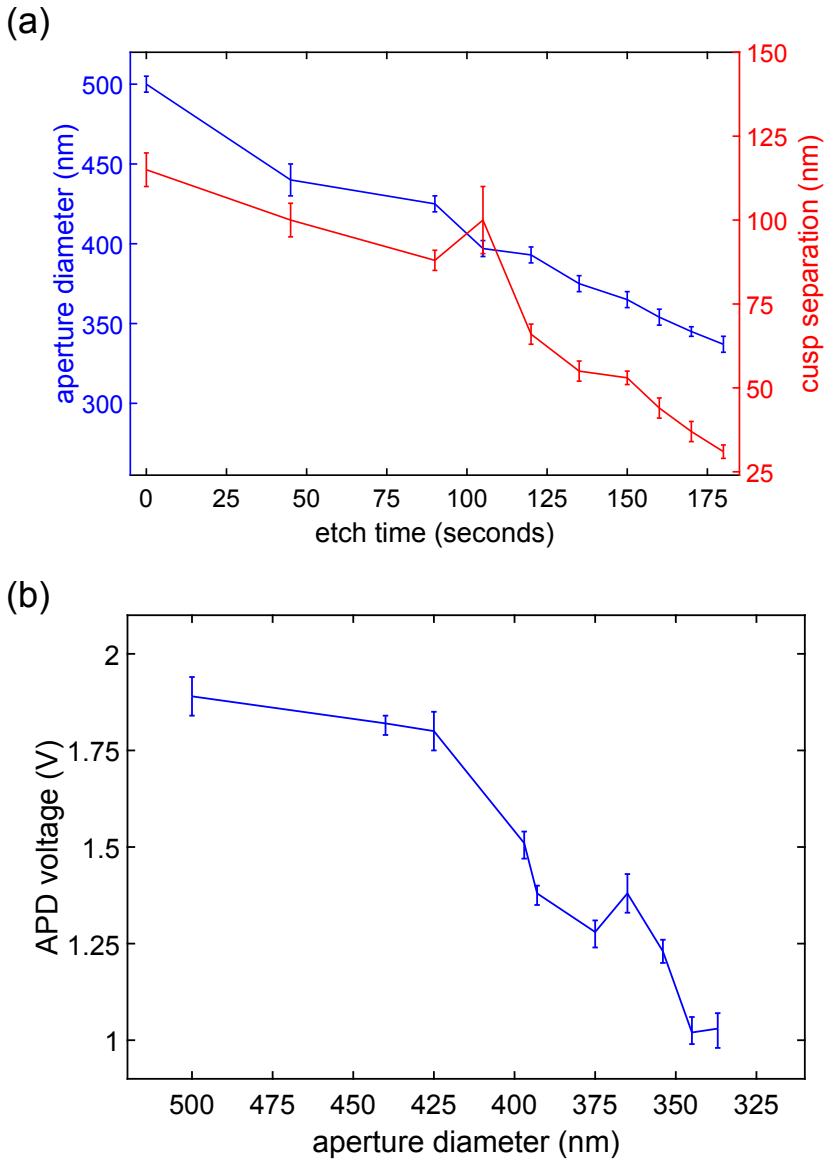

Figure 4.12: (a) Effect of plasma etching on the double-nanohole dimensions fabricated using 500 nm polystyrene spheres. (b) Transmission measurements through apertures fabricated using 500 nm polystyrene spheres [1].

Figure 4.8 (a) shows the effect of plasma etching on the aperture diameter and cusp separation for various double-nanohole apertures fabricated using 200 nm polystyrene spheres. At the start of the plasma etching process, surface reflow between polystyrene beads increases the cusp separation. Continuing the plasma etching process eventually decreases cusp separation. A steady decrease in the aperture diameter is observed due to an almost uniform surface etching of polystyrene spheres. Figure 4.8 (b) shows the variation in transmission through the different apertures when illuminated with a focused 980 nm laser, polarization adjusted for maximum transmission. The transmission characteristics indicate a non-monotonic behavior that could be associated with the tuning of plasmonic resonances with varying aperture dimensions. The error bar indicates variation in measurements from multiple double-nanohole apertures for a given etch time.

Figure 4.9 shows the various double-nanohole apertures with different dimensions fabricated with 300 nm polystyrene spheres using the combined colloidal lithography and plasma etching technique. Figure 4.10 (a) shows the effect of plasma etching on the aperture diameter and cusp separation of these fabricated apertures. Figure 4.10 (b) shows the variation in transmission through the different apertures when illuminated with a focused 980 nm laser, polarization adjusted for maximum transmission. The transmission characteristics indicate a non-monotonic behaviour similar to apertures fabricated using the 200 nm spheres. This is proposed to arise from the tuning

of plasmonic resonances with the change in dimensions. Similarly, fabrication and characterization were carried out using polystyrene spheres of diameter 500 nm. The fabricated apertures are shown in Figure 4.11. Figure 4.12 (a) indicates the tuning of the aperture dimensions. A delayed onset of reflow and increase in cusp separation is observed. The variation in transmission through the apertures is depicted in Figure 4.12 (b).

4.3 Trapping

Before commencing the measurement for an optical trapping experiment, the setup is calibrated. Maximum transmission is verified on the APD prior to initiating any measurement. If it is turned off, the APD may require a warm-up time (around 30 minutes) for stabilizing the voltage reading after switching it back on. Once the pre-experiment setup check is complete, a sample with the analyte needs to be prepared. A suitable glass cover slide with a thickness of about 150 μm (Ted Pella, Inc.) and an imaging spacer (Secure Seal, Grace Bio-labs) attached to the center of the slide help create a micro-well (thickness of 120 μm and a 9 mm diameter). A micro-pipette is used for transferring $\sim$ 20 μL of the analyte into the micro-well, which is sealed using one of the gold samples with the fabricated apertures. The tip of the fiduciary mark on the gold sample is ensured to be in the center of the micro-well. The various

aspects of the sample prepared for optical trapping are depicted in Figure 4.13. Ensuring the uniform adhesion of the imaging spacer on the glass cover slide and using an additional quantity of the analyte help prevent air bubbles from forming in the micro-well during the sample preparation. If formed, the air bubbles prevent proper measurement during the experiment and require a remaking of the sample. To remove the fabricated sample attached to the cover slide requires soaking the sample in an acetone bath for $\sim$ 10 minutes following which it can be placed on a hard surface and then separated using a twisting motion. The details of the different particles used in the analyte are given in table 4.1.

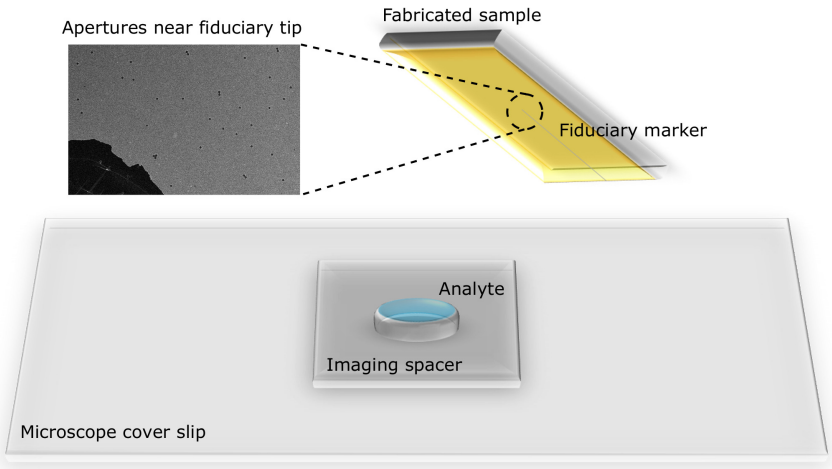

Figure 4.13: Various components of a sample used in an optical trapping experiment.

Once the sample is prepared, it is placed on the sample holder in the optical trapping setup in between the objectives. A drop of immersion oil, with refractive index of 1.51, is applied on the glass cover slide region below the micro-well. Excess use of oil can cause the sample to slip, preventing precise positioning and causing undesired variation in measurement. The sample is placed on the sample holder with the glass cover slide facing the oil immersion objective. It is important to wipe the oil immersion objective clean, using a lens wipe, before and after use to prevent any residual oil from affecting the current measurement.

Table 4.1: Particle specification

Particle ⊕ *Parameter*	PS	Rubisco	BSA
Dimensions	30 nm ± 4 nm (diameter)	6.5 nm × 7.1 nm × 10.4 nm	14 nm × 4 nm × 4 nm
Molecular weight	104.1 g/mol	560 kg/mol	66.5 kg/mol
Manufacturer (or supplier)	Thermo Fisher	Sigma Aldrich	Sigma Aldrich
Concentration $(w/v)^*$ used for trapping	1%	0.6%	2%
Solvent	Water	1×PBS	1×PBS

* *(w)eight of solute/(v)olume of solvent* (g/mL) = *molecular weight* (g/mol) * *molarity* (mol/L) * $10^{-}3$.

After the sample is placed, the white light source on the setup is switched on to view the location of the nanoapertures imaged by the bottom CCD. First, the fiduciary marker is located and brought into focus by adjusting the z-height of the stage. Next, it is ensured that the appropriate parameters for the laser diode operation are configured on the laser controller, especially the current limit, to prevent any damage to the source. The laser is then switched on. Finally, the 3-axis piezoelectric stage with 20 nm translation precision is used for aligning the position of the aperture on the sample. Fine focus and z-height using the piezo controller, as well as the polarization tuned by the HWP is critical to the quality of measurements.

Figure 4.14 shows trapping events for a 30 nm polystyrene sphere. Marker A indicates the signal recorded by the APD when the white light source for imaging the aperture is switched on. Marker B shows the signal level when the trapping laser is unblocked and illuminates the aperture. The APD signal recorded when the laser is unblocked represents the untrapped state when there is no particle trapped in the aperture. The voltage jump at marker C with increased noise levels is the instance when a polystyrene nanosphere is trapped. The variations in noise in the trapped state arise from the random motion of the particle within the trap or conformations and structural changes within the particle. A magnified view of the trapping event is shown in the inset. The laser should be blocked to untrap the particle in the trapped state. When the laser is blocked, the white light source remains switched on. Sub-

sequently, the white light source is switched off and switched on back again followed by unblocking the laser. It is necessary to block the laser to release the particle since the SIBA comes into effect when the particle tries to move away from the trap.

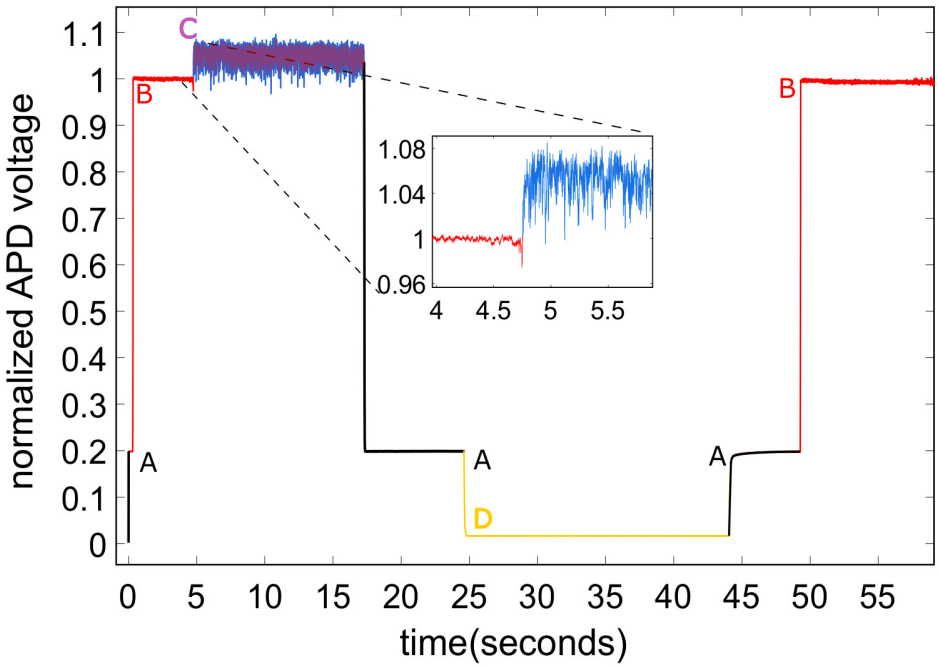

Figure 4.14: Trapping events of a 30 nm polystyrene sphere [1]. Marker A: indicates white light switched on and laser switched off, B: laser and white light switched on, C: particle trapped and D: white light switched off.

Figure 4.15 shows the trapping of a rubisco enzyme and Figure 4.16 shows the trapping of a BSA protein. In both the events, the white light source is switched on at A, followed by unblocking the laser at B. The trapping of the respective particles is

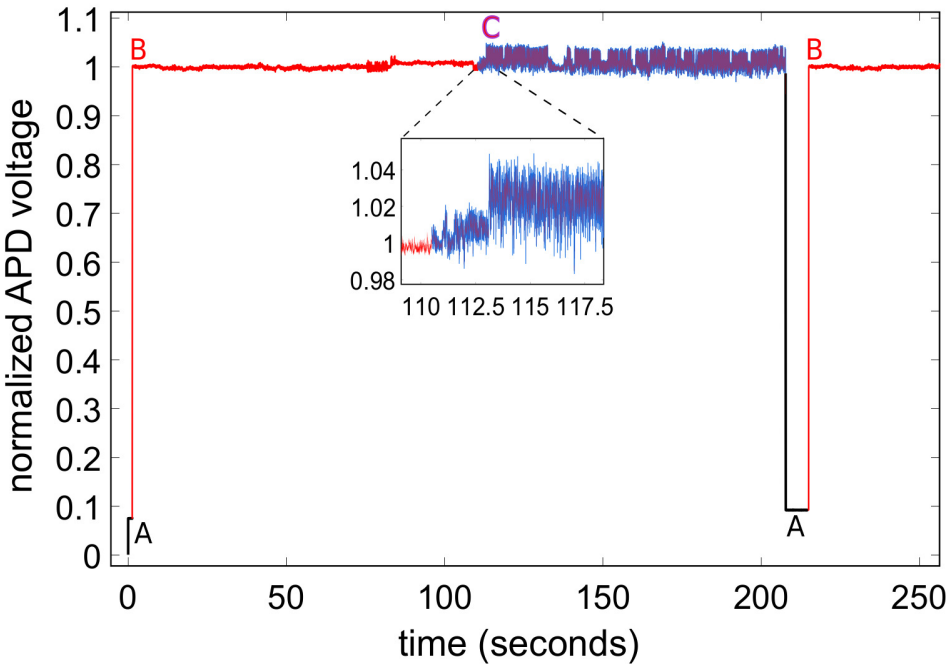

Figure 4.15: Trapping events of rubisco [1]. Marker A: indicates white light switched on and laser switched off, B: laser and white light switched on and C: particle trapped.

indicated by marker C, magnified in the inset. The laser is then blocked to release the trapped particle shown by the untrapped state B. This process of trapping and untrapping a particle upon unblocking and blocking the laser is seen repeatedly and reliably throughout the experiment.

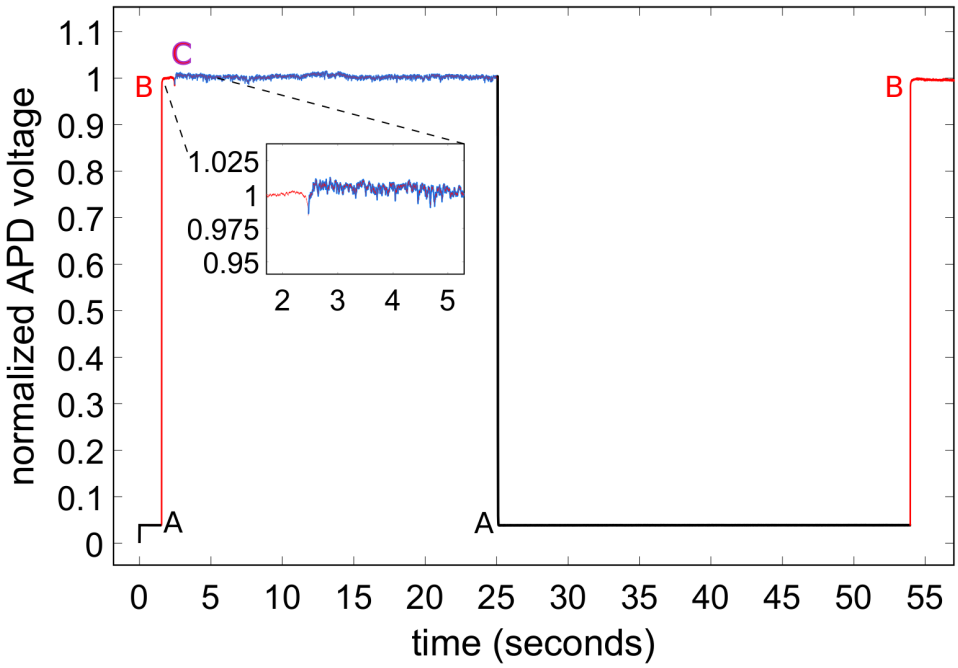

Figure 4.16: Trapping events of BSA [1]. Marker A: indicates white light switched on and laser switched off, B: laser and white light switched on and C: particle trapped.

Chapter 5

FDTD Simulations

For nuanced nanostructures like the double-nanohole aperture, solutions to Maxwell's equations are essential to obtain a theoretical estimation of parameters such as the transmitted field intensity. The most widely adopted numerical analysis method for computational electrodynamics is the FDTD method. This technique solves Maxwell's equations by resolving regions into discrete spatial and temporal cartesian grids. A commercially available FDTD software suite from Lumerical Inc. was utilized to calculate the transmission through double-nanohole apertures. FDTD simulation results of transmitted field intensity for double-nanohole apertures with dimensions obtained from fabrication using 200 nm, 300 nm and 500 nm polystyrene spheres are presented in this Chapter.

5.1 Design Considerations

Appropriate design practices are implemented for accurate analysis using FDTD simulations. Various aspects of simulation design are discussed in the following sections.

5.1.1 Meshing

Rectangular meshes are used in FDTD simulations. The simulation quantities are calculated at each mesh point. Convergence tests are carried out to ensure that appropriate mesh dimensions are selected for accurate calculations. For structural features requiring priority in overlapping or need etching, the mesh order parameter is used. A lower mesh order number has priority over a higher mesh order number.

5.1.2 Boundary Conditions

There are various boundary types that can encompass a simulation region. Usually, a perfectly-matched layer (PML) boundary is employed to prevent reflections. PML boundaries absorb incident electromagnetic fields by modelling as reflectionless boundaries. They are of a finite thickness within which the absorption of light occurs. The boundaries are impedance matched to the materials in the simulation region that

extend beyond them.

Smaller mesh dimensions can be chosen to improve the accuracy of the simulation. This necessitates a trade-off between memory requirements and machine resources. Boundary conditions with symmetry, if present, are helpful in reducing the simulation time by a factor of 2 for every applicable coordinate direction. Symmetry is true when a plane of symmetry exists in the simulation region. If the electric field component is tangential to a boundary plane with symmetry in that particular coordinate direction, the symmetric boundary condition is valid. Similarly, if the electric field component is normal to the boundary plane with symmetry in a particular coordinate direction, an anti-symmetric boundary condition is valid.

5.1.3 Sources

Choosing an appropriate source is critical to FDTD simulations. Different sources are available depending on the simulation objective and design parameters. For example, a plane wave source cannot be used over a PML boundary as it is assumed to be unbounded in space and can create artifacts during the interaction at the boundary. A Gaussian source modelled by a Gaussian spatial intensity profile can be used with PML boundaries since the intensity decays to nearly zero at the boundary and interactions at PML boundaries is minimized.

The most appropriate source to use with PML boundaries has been found to be a total-field scattered-field (TFSF) source. The TFSF separates the simulation region into a total-field region and a scattered-field region. The total-field region contains the sum of the incident field and scattered-field, whereas, the scattered-field region contains only the scattered field. For a TFSF source, the incident electromagnetic field is modelled as a plane wave with its wave vector normal to the surface from which it propagates and is especially useful for studying scattering characteristics.

5.1.4 Monitors

To accurately capture the field profile within a simulation region, frequency-domain monitors are extremely useful. To restrict memory use, desired frequency points can be kept to a minimum. Additionally, specifying only required parameters that need calculating and disabling others helps restrict memory use.

5.2 Simulation Design and Results

Transmission characteristics of various double-nanohole apertures, with dimensions as obtained using the colloidal lithography technique, were analyzed using FDTD simulations and compared with the results measured experimentally. In order to make the

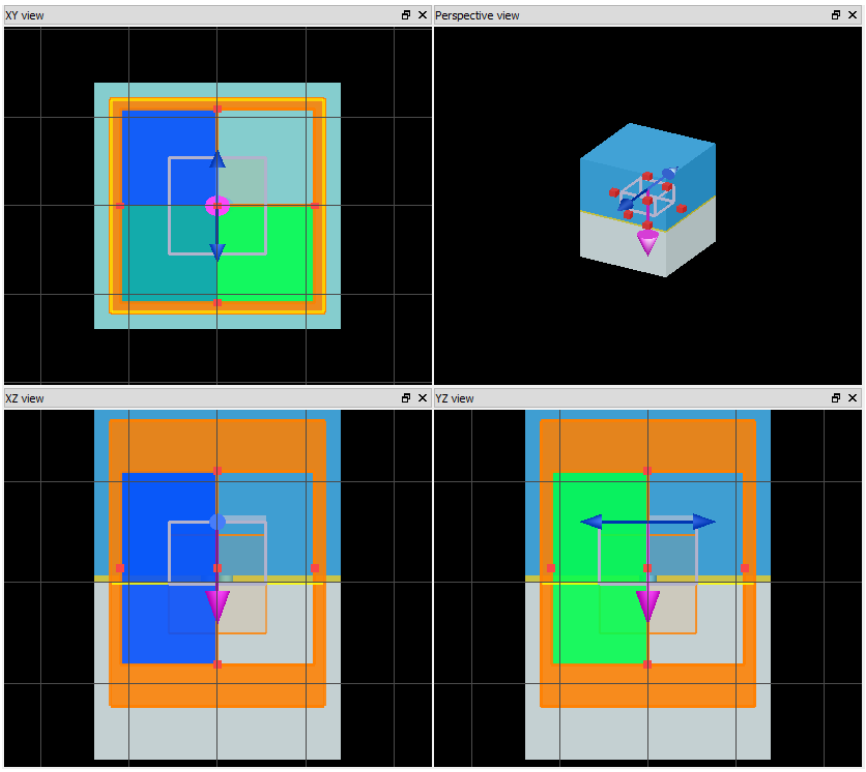

Figure 5.1: FDTD simulation design configuration for calculating transmission through a double-nanohole aperture. The figure shows different perspective views of the simulation region.

study as accurate as possible, the simulation configuration was designed to mimic the experimental arrangement. In experimental measurement, the transmission is measured through a sample made up of multiple layers. It consists of a 1 mm thick glass substrate with a sputtered gold layer, of thickness 70 nm, sealing a layer of water in a micro-well, of thickness 120 μm, adhered on a glass cover slide.

For accurate design, the material for the glass substrate is chosen as SiO_2 (Glass) - Palik [62] from the materials tab. The thickness of this layer is chosen to be 1.75 μm with lateral dimensions of 2.8 μm$\times$2.8 μm. The thickness of the glass layer is sufficient to model an optically dense glass layer allowing an adequate gold interface region to be enclosed within the FDTD boundaries. A layer of Au (Gold) - Palik material above the glass layer with a 70 nm thickness and lateral dimensions matching the glass layer is created to model the gold layer in the sample. Similar to experiments, a 2 μm thick layer of water (material H_2O (Water) - Palik) is placed above the gold layer. The lateral dimensions are the same as the gold and glass layers. A double-nanohole aperture is modelled as two cylinders of thickness 70 nm etched into the gold layer by selecting the mesh order as zero. The aperture material is selected as water. The dimensions of the aperture diameter and cusp separation are ensured to match the fabricated apertures. The overlap of the two circular apertures is adjusted manually to obtain accurate cusp separations.

To model the laser source, a TFSF source, with a wavelength of excitation ranging from 880 nm to 1080 nm, is configured. The source is placed at a distance of 600 nm on top of the gold layer. The length and width of the TFSF source are each selected to be 1.1 μm to model a focused beam replicated in the trapping setup. The polarization of the light source is selected to be along the axis of the cusps of the double-nanohole structure for maximum transmission. A frequency-domain power monitor is placed 100 nm below the gold layer to measure the transmission. The lateral dimensions of the monitor are set to 2.4 μm$\times$2.4 μm. An FDTD region with dimensions 2.8 μm$\times$2.8 μm$\times$1.91 μm is created around the simulation setup with PML boundary symmetry conditions selected. The distance of the FDTD boundaries from the TFSF source boundaries is ensured to be at least half the maximum wavelength of the source. A mesh with dimensions 1.1 μm$\times$1.1 μm$\times$0.97 μm is configured, and simulations are run with mesh unit sizes of 5 nm and 1 nm.

The simulation results shown in Figure 5.2 depict the transmission characteristics for apertures with dimensions obtained from fabrication with 200 nm polystyrene spheres. The variation in the transmission is predicted to arise from the tuning of plasmonic resonance with the change in aperture dimensions. The oscillating behaviour follows a similar trend observed in experimental measurements.

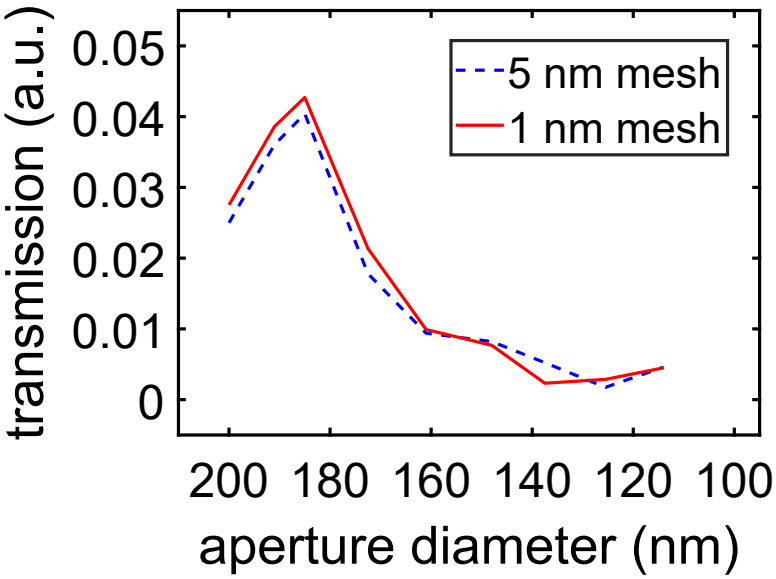

Figure 5.2: FDTD simulation results for transmission through double-nanohole apertures with dimensions as obtained from fabrication with 200 nm polystyrene spheres. The simulation results for both 5 nm and 1 nm mesh configurations are depicted.

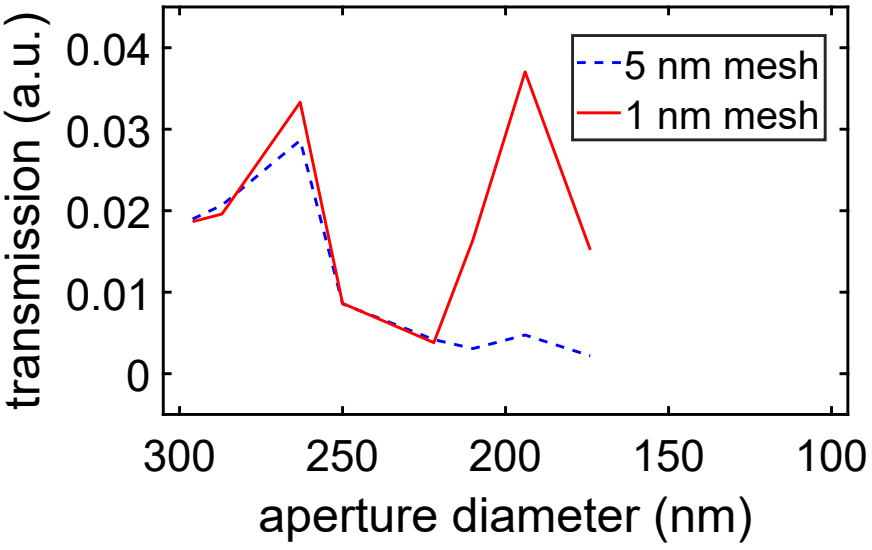

Figure 5.3: FDTD simulation results for transmission through double-nanohole apertures with dimensions as obtained from fabrication with 300 nm polystyrene spheres. The simulation results for both 5 nm and 1 nm mesh configurations are depicted.

Results depicted in Figure 5.3 and Figure 5.4 indicate non-monotonic transmission characteristics from apertures fabricated with 300 nm and 500 nm polystyrene spheres supporting the behaviour established by experimental data and appear to be systematic regardless of aperture size.

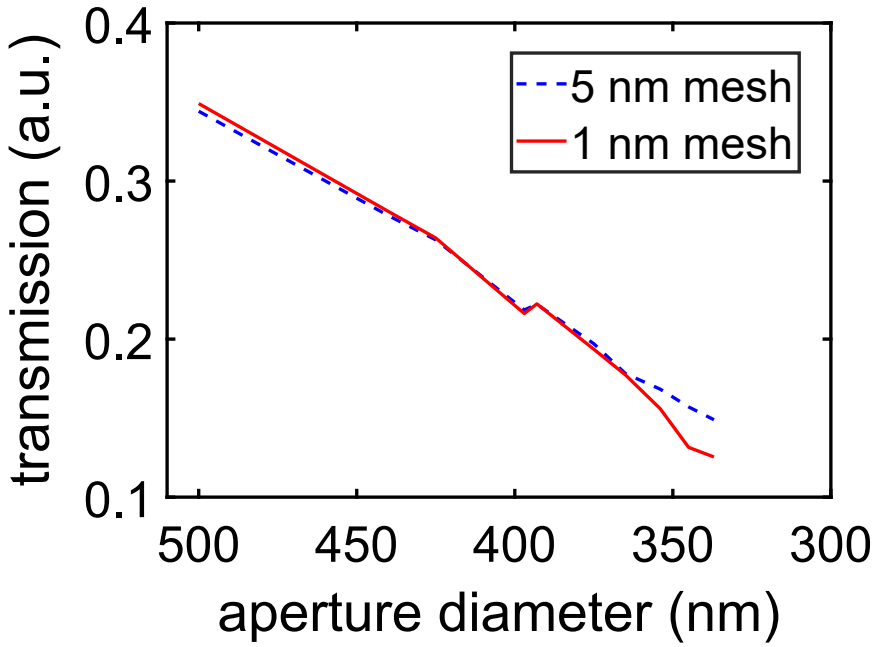

Figure 5.4: FDTD simulation results for transmission through double-nanohole apertures with dimensions as obtained from fabrication with 500 nm polystyrene spheres. The simulation results for both 5 nm and 1 nm mesh configurations are depicted.

Theoretical calculations for transmission from FDTD simulations appear to be in qualitative agreement with experimentally observed measurements for most aperture dimensions. The local maxima in the transmission measured through apertures fab-

ricated using the 200 nm polystyrene spheres from experiments occur around etched diameters of 180 nm, 160 nm and 120 nm (Figure 4.8(b)), whereas, the maxima from simulations are located around etched diameters of 180 nm, 150 nm and 110 nm (Figure 5.2). A similar agreement is observed for apertures fabricated with 300 nm polystyrene spheres. Peaks appear around aperture diameters of 260 nm and 190 nm in both experiments (Figure 4.10(b)) and simulations (Figure 5.3). In the case of apertures fabricated with 500 nm polystyrene spheres, a maximum is observed at 360 nm from experiments (Figure 4.12(b)) with simulations indicating a maximum at 390 nm (Figure 5.4).

Chapter 6

Conclusion and Future Work

This thesis provides an overview of optical trapping using conventional methods and introduces plasmonic double-nanohole optical trapping as a solution to overcome existing limitations. Fabrication of double-nanohole apertures using bottom-up colloidal lithography technique is considered to be a cost-effective high-throughput alternative to conventional top-down methods and proven through supporting experiments. Improvements to the experimental setup are discussed with results indicating better quality of measurements. Additional modifications to the setup enable different types of measurements. This makes it possible to perform various kinds experiments.

Dimensions of the apertures fabricated using colloidal lithography are tuned through plasma etching polystyrene sphere dimers formed during the fabrication process. The tuning of aperture diameter and cusp separation is a key component in the fabrication

phase. The polarization dependence of a double-nanohole aperture is performed and compared with a theoretical prediction. Furthermore, transmission characterization studies of apertures fabricated using different polystyrene sphere sizes of 200 nm, 300 nm and 500 nm were carried out. The existence of plasmonic resonances with varying shapes is predicted and is reinforced by observation of non-monotonic transmission behaviour from computational electrodynamics simulations using Lumerical FDTD software. Additionally, results from optical trapping of nanoparticles, enzymes and proteins are presented, validating the effectiveness of double-nanohole apertures fabricated using the colloidal lithography technique. This technique is expected to redefine the future research efforts in plasmonic nanoaperture optical trapping.

Future work is expected to be pursued on optimizing aperture dimensions in accordance with the wavelength of operation. White light spectroscopy studies on apertures can be performed as a preliminary step. Additionally, optical trapping of particles using various shapes like trimers and larger assemblies, shown in Figure 6.1, could be carried out. Improvements to current work can be achieved by adopting a template-directed assembly of structures placed deterministically at a specific location by including imprint or photolithography as an additional step in the fabrication process [63, 49].

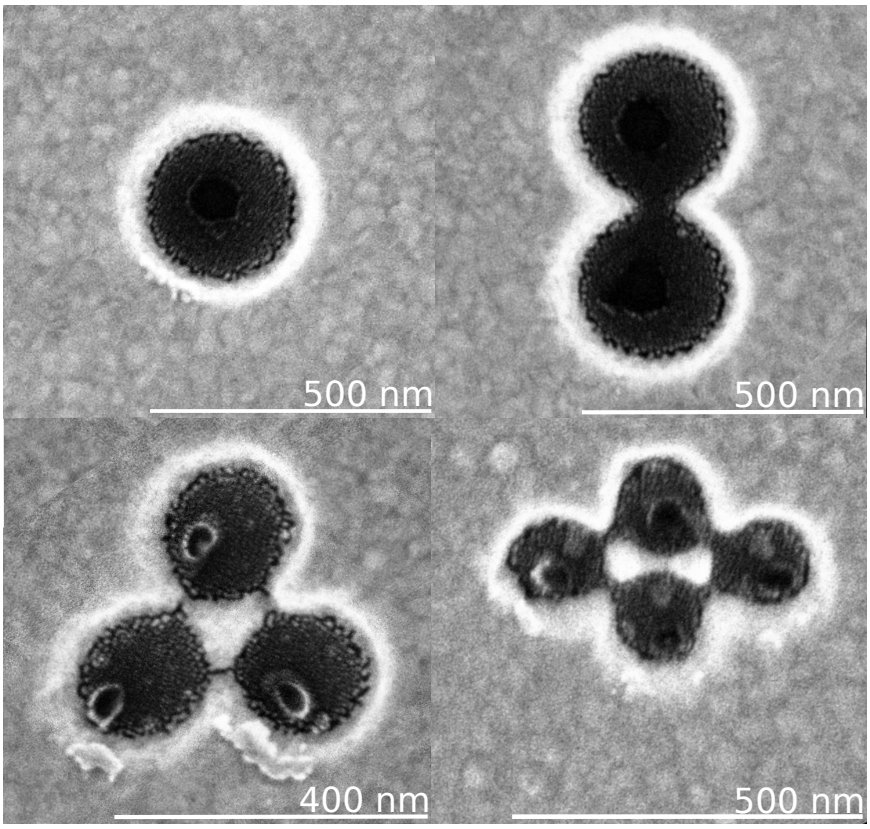

Figure 6.1: Various apertures fabricated by the colloidal lithography technique.

Another interesting direction of research could be in combining the fabrication approach of colloidal lithography with nanopores for a complimentary analysis. Nanopores have recently been integrated with apertures to analyze proteins and DNA [64, 65, 66] as well as used in studying their properties by ionic-flow analysis [67]. More generally, nanopores have been used in investigating single proteins [68, 69, 70], DNA [71, 72, 73, 74, 75, 76, 77] and protein-DNA interactions [78, 79] in flow-through translocation [80]. Light-assisted self-aligned breakdown might be adopted [81] to obtain the nanopore between the cusps of a double-nanohole aperture. The technique of colloidal lithography double-nanohole optical trapping has proven to be an effective tool for single-molecular studies and the work presented in the thesis is expected to be a step towards the future of optical trapping research.

Bibliography

[1] Adarsh Lalitha Ravindranath, Mirali Seyed Shariatdoust, Samuel Mathew, and Reuven Gordon. Colloidal lithography double-nanohole optical trapping of nanoparticles and proteins. *Opt. Express*, 27(11):16184–16194, May 2019.

[2] Arthur Ashkin. History of optical trapping and manipulation of small-neutral particle, atoms, and molecules. *IEEE Journal of Selected Topics in Quantum Electronics*, 6(6):841–856, 2000.

[3] Steven Chu. Nobel lecture: The manipulation of neutral particles. *Reviews of Modern Physics*, 70(3):685, 1998.

[4] Arthur Ashkin, James M Dziedzic, JE Bjorkholm, and Steven Chu. Observation of a single-beam gradient force optical trap for dielectric particles. *Optics Letters*, 11(5):288–290, 1986.

[5] Arthur Ashkin. Trapping of atoms by resonance radiation pressure. *Physical Review Letters*, 40(12):729, 1978.

[6] Arthur Ashkin. Acceleration and trapping of particles by radiation pressure. *Physical review letters*, 24(4):156, 1970.

[7] Arthur Ashkin and JM Dziedzic. Optical levitation by radiation pressure. *Applied Physics Letters*, 19(8):283–285, 1971.

[8] Steven Chu, L. Hollberg, J. E. Bjorkholm, A. Cable, and A. Ashkin. Three-dimensional viscous confinement and cooling of atoms by resonance radiation pressure. *Phys. Rev. Lett.*, 55:48–51, Jul 1985.

[9] Steven Chu, J. E. Bjorkholm, A. Ashkin, and A. Cable. Experimental observation of optically trapped atoms. *Phys. Rev. Lett.*, 57:314–317, Jul 1986.

[10] E. L. Raab, M. Prentiss, Alex Cable, Steven Chu, and D. E. Pritchard. Trapping of neutral sodium atoms with radiation pressure. *Phys. Rev. Lett.*, 59:2631–2634, Dec 1987.

[11] Arthur Ashkin and James M Dziedzic. Optical trapping and manipulation of viruses and bacteria. *Science*, 235(4795):1517–1520, 1987.

[12] A Ashkin and JM Dziedzic. Internal cell manipulation using infrared laser traps. *Proceedings of the National Academy of Sciences*, 86(20):7914–7918, 1989.

[13] Ali Khademi, Timothy Dewolf, and Reuven Gordon. Quantum plasmonic epsilon near zero: field enhancement and cloaking. *Optics express*, 26(12):15656–15664, 2018.

[14] Lukas Novotny, Randy X Bian, and X Sunney Xie. Theory of nanometric optical tweezers. *Physical Review Letters*, 79(4):645, 1997.

[15] K Okamoto and S Kawata. Radiation force exerted on subwavelength particles near a nanoaperture. *Physical review letters*, 83(22):4534, 1999.

[16] Eun-Soo Kwak, Tiberiu-Dan Onuta, Dragos Amarie, Radislav Potyrailo, Barry Stein, Stephen C Jacobson, WL Schaich, and Bogdan Dragnea. Optical trapping with integrated near-field apertures. *The Journal of Physical Chemistry B*, 108(36):13607–13612, 2004.

[17] Mathieu L Juan, Reuven Gordon, Yuanjie Pang, Fatima Eftekhari, and Romain Quidant. Self-induced back-action optical trapping of dielectric nanoparticles. *Nature Physics*, 5(12):915, 2009.

[18] Eric X Jin and Xianfan Xu. Enhanced optical near field from a bowtie aperture. *Applied physics letters*, 88(15):153110, 2006.

[19] J Berthelot, SS Aćimović, ML Juan, MP Kreuzer, J Renger, and R Quidant. Three-dimensional manipulation with scanning near-field optical nanotweezers. *Nature nanotechnology*, 9(4):295, 2014.

[20] Russell A Jensen, I-Chun Huang, Ou Chen, Jennifer T Choy, Thomas S Bischof, Marko Loncar, and Moungi G Bawendi. Optical trapping and two-photon excita-

tion of colloidal quantum dots using bowtie apertures. *ACS Photonics*, 3(3):423–427, 2016.

[21] Chang Chen, Mathieu L Juan, Yi Li, Guido Maes, Gustaaf Borghs, Pol Van Dorpe, and Romain Quidant. Enhanced optical trapping and arrangement of nano-objects in a plasmonic nanocavity. *Nano letters*, 12(1):125–132, 2011.

[22] Amr AE Saleh and Jennifer A Dionne. Toward efficient optical trapping of sub-10-nm particles with coaxial plasmonic apertures. *Nano letters*, 12(11):5581–5586, 2012.

[23] Daehan Yoo, Kargal L Gurunatha, Han-Kyu Choi, Daniel A Mohr, Christopher T Ertsgaard, Reuven Gordon, and Sang-Hyun Oh. Low-power optical trapping of nanoparticles and proteins with resonant coaxial nanoaperture using 10 nm gap. *Nano letters*, 18(6):3637–3642, 2018.

[24] M Righini, P Ghenuche, S Cherukulappurath, Viktor Myroshnychenko, Francisco Javier García de Abajo, and Romain Quidant. Nano-optical trapping of rayleigh particles and escherichia coli bacteria with resonant optical antennas. *Nano letters*, 9(10):3387–3391, 2009.

[25] Weihua Zhang, Lina Huang, Christian Santschi, and Olivier JF Martin. Trapping and sensing 10 nm metal nanoparticles using plasmonic dipole antennas. *Nano letters*, 10(3):1006–1011, 2010.

[26] Brian J Roxworthy, Kaspar D Ko, Anil Kumar, Kin Hung Fung, Edmond KC Chow, Gang Logan Liu, Nicholas X Fang, and Kimani C Toussaint Jr. Application of plasmonic bowtie nanoantenna arrays for optical trapping, stacking, and sorting. *Nano Letters*, 12(2):796–801, 2012.

[27] Reuven Gordon. Nanostructured metals for light-based technologies. *Nanotechnology*, 30(21):212001, 2019.

[28] Antoine Lesuffleur, L Kiran Swaroop Kumar, and Reuven Gordon. Enhanced second harmonic generation from nanoscale double-hole arrays in a gold film. *Applied physics letters*, 88(26):261104, 2006.

[29] L Kiran Swaroop Kumar and Reuven Gordon. Overlapping double-hole nanostructure in a metal film for localized field enhancement. *IEEE Journal of selected topics in quantum electronics*, 12(6):1228–1232, 2006.

[30] LKS Kumar, A Lesuffleur, MC Hughes, and R Gordon. Double nanohole apex-enhanced transmission in metal films. *Applied Physics B*, 84(1-2):25, 2006.

[31] A Lesuffleur, LKS Kumar, AG Brolo, KL Kavanagh, and R Gordon. Apex-enhanced raman spectroscopy using double-hole arrays in a gold film. *The Journal of Physical Chemistry C*, 111(6):2347–2350, 2007.

[32] Yuanjie Pang and Reuven Gordon. Optical trapping of 12 nm dielectric spheres using double-nanoholes in a gold film. *Nano letters*, 11(9):3763–3767, 2011.

[33] Yuanjie Pang and Reuven Gordon. Optical trapping of a single protein. *Nano letters*, 12(1):402–406, 2011.

[34] Yuanjie Pang. *Nanophotonics with subwavelength apertures: theories and applications.* PhD thesis, University of Victoria, 2012.

[35] Abhay Kotnala and Reuven Gordon. Double nanohole optical tweezers visualize protein p53 suppressing unzipping of single dna-hairpins. *Biomedical optics express*, 5(6):1886–1894, 2014.

[36] Abhay Kotnala. *Double Nanohole Optical Tweezer for Single Molecule and Nanoparticle Analysis*. PhD thesis, University of Victoria, 2015.

[37] Skyler Wheaton, Ryan M Gelfand, and Reuven Gordon. Probing the raman-active acoustic vibrations of nanoparticles with extraordinary spectral resolution. *Nature Photonics*, 9(1):68, 2015.

[38] Abhay Kotnala, Skyler Wheaton, and Reuven Gordon. Playing the notes of dna with light: extremely high frequency nanomechanical oscillations. *Nanoscale*, 7(6):2295–2300, 2015.

[39] Steven Jones. Characterization of single nanoparticles. Master's thesis, University of Victoria, 2016.

[40] Skyler Wheaton and Reuven Gordon. Molecular weight characterization of single globular proteins using optical nanotweezers. *Analyst*, 140(14):4799–4803, 2015.

[41] Noa Hacohen, Candice JX Ip, and Reuven Gordon. Analysis of egg white protein composition with double nanohole optical tweezers. *ACS Omega*, 3(5):5266–5272, 2018.

[42] Noa Hacohen. Characterization of single proteins using double nanohole optical tweezers. Master's thesis, University of Victoria, 2018.

[43] Yuanyuan Chen, Abhay Kotnala, Li Yu, Jiasen Zhang, and Reuven Gordon. Wedge and gap plasmonic resonances in double nanoholes. *Optics express*, 23(23):30227–30236, 2015.

[44] Yuanjie Pang and Reuven Gordon. Nanophotonics using a subwavelength aperture in a metal film. *Nanotechnology Reviews*, 1(4):339–362, 2012.

[45] Reuven Gordon. Biosensing with nanoaperture optical tweezers. *Optics & Laser Technology*, 109:328–335, 2019.

[46] Thomas W Ebbesen, Henri J Lezec, HF Ghaemi, Tineke Thio, and Peter A Wolff. Extraordinary optical transmission through sub-wavelength hole arrays. *Nature*, 391(6668):667, 1998.

[47] Prashant Nagpal, Nathan C Lindquist, Sang-Hyun Oh, and David J Norris. Ultrasmooth patterned metals for plasmonics and metamaterials. *Science*, 325(5940):594–597, 2009.

[48] Ana Zehtabi-Oskuie, Aurora A Zinck, Ryan M Gelfand, and Reuven Gordon. Template stripped double nanohole in a gold film for nano-optical tweezers. *Nanotechnology*, 25(49):495301, 2014.

[49] Gang Zhang and Dayang Wang. Colloidal lithography — the art of nanochemical patterning. *Chemistry–An Asian Journal*, 4(2):236–245, 2009.

[50] U Ch Fischer and Hans P Zingsheim. Submicroscopic pattern replication with visible light. *Journal of Vacuum Science and Technology*, 19(4):881–885, 1981.

[51] HW Deckman and JH Dunsmuir. Natural lithography. *Applied Physics Letters*, 41(4):377–379, 1982.

[52] John C Hulteen and Richard P Van Duyne. Nanosphere lithography: A materials general fabrication process for periodic particle array surfaces. *Journal of Vacuum Science & Technology A: Vacuum, Surfaces, and Films*, 13(3):1553–1558, 1995.

[53] Christy L. Haynes and Richard P. Van Duyne. Nanosphere lithography: a versatile nanofabrication tool for studies of size-dependent nanoparticle optics. *The Journal of Physical Chemistry B*, 105(24):5599–5611, 2001.

[54] Seung-Man Yang, Se Gyu Jang, Dae-Geun Choi, Sarah Kim, and Hyung Kyun Yu. Nanomachining by colloidal lithography. *Small*, 2(4):458–475, 2006.

[55] Alfred Plettl, Fabian Enderle, Marc Saitner, Achim Manzke, Christian Pfahler, Stefan Wiedemann, and Paul Ziemann. Non-close-packed crystals from self-assembled polystyrene spheres by isotropic plasma etching: Adding flexibility to colloid lithography. *Advanced Functional Materials*, 19(20):3279–3284, 2009.

[56] Si Hoon Lee, Kyle C Bantz, Nathan C Lindquist, Sang-Hyun Oh, and Christy L Haynes. Self-assembled plasmonic nanohole arrays. *Langmuir*, 25(23):13685–13693, 2009.

[57] Marie-Pier Murray-Méthot, Mathieu Ratel, and Jean-Francois Masson. Optical properties of Au, Ag, and bimetallic Au on Ag nanohole arrays. *The Journal of Physical Chemistry C*, 114(18):8268–8275, 2010.

[58] Jean-François Masson, Marie-Pier Murray-Méthot, and Ludovic S Live. Nanohole arrays in chemical analysis: manufacturing methods and applications. *Analyst*, 135(7):1483–1489, 2010.

[59] U Ch Fischer. Optical characteristics of 0.1 μm circular apertures in a metal film as light sources for scanning ultramicroscopy. *Journal of Vacuum Science & Technology B: Microelectronics Processing and Phenomena*, 3(1):386–390, 1985.

[60] U Ch Fischer. Submicrometer aperture in a thin metal film as a probe of its microenvironment through enhanced light scattering and fluorescence. *JOSA B*, 3(10):1239–1244, 1986.

[61] Tiberiu-Dan Onuta, Matthias Waegele, Christopher C DuFort, William L Schaich, and Bogdan Dragnea. Optical field enhancement at cusps between adjacent nanoapertures. *Nano Letters*, 7(3):557–564, 2007.

[62] Edward D Palik. *Handbook of optical constants of solids*, volume 3. Academic press, 1998.

[63] Dayang Wang and Helmuth Möhwald. Template-directed colloidal self-assembly–the route to 'top-down'nanochemical engineering. *Journal of Materials Chemistry*, 14(4):459–468, 2004.

[64] Maxim Belkin, Shu-Han Chao, Magnus P Jonsson, Cees Dekker, and Aleksei Aksimentiev. Plasmonic nanopores for trapping, controlling displacement, and sequencing of dna. *ACS Nano*, 9(11):10598–10611, 2015.

[65] Daniel Verschueren, Xin Shi, and Cees Dekker. Nano-optical tweezing of single proteins in plasmonic nanopores. *Small Methods*, page 1800465, 2019.

[66] Daniel V Verschueren, Sergii Pud, Xin Shi, Lorenzo De Angelis, L Kuipers, and Cees Dekker. Label-free optical detection of dna translocations through plasmonic nanopores. *ACS nano*, 13(1):61–70, 2018.

[67] Zachary Roelen, José A Bustamante, Autumn Carlsen, Aidan Baker-Murray, and Vincent Tabard-Cossa. Instrumentation for low noise nanopore-based ionic

current recording under laser illumination. *Review of Scientific Instruments*, 89(1):015007, 2018.

[68] Erik C Yusko, Jay M Johnson, Sheereen Majd, Panchika Prangkio, Ryan C Rollings, Jiali Li, Jerry Yang, and Michael Mayer. Controlling protein translocation through nanopores with bio-inspired fluid walls. *Nature Nanotechnology*, 6(4):253, 2011.

[69] Wenhong Li, Nicholas AW Bell, Silvia Hernández-Ainsa, Vivek V Thacker, Alana M Thackray, Raymond Bujdoso, and Ulrich F Keyser. Single protein molecule detection by glass nanopores. *ACS Nano*, 7(5):4129–4134, 2013.

[70] Erik C Yusko, Brandon R Bruhn, Olivia M Eggenberger, Jared Houghtaling, Ryan C Rollings, Nathan C Walsh, Santoshi Nandivada, Mariya Pindrus, Adam R Hall, David Sept, Jiali Li, Devendra S Kalonia, and Michael Mayer. Real-time shape approximation and fingerprinting of single proteins using a nanopore. *Nature Nanotechnology*, 12(4):360, 2017.

[71] Stefan Howorka, Stephen Cheley, and Hagan Bayley. Sequence-specific detection of individual dna strands using engineered nanopores. *Nature Biotechnology*, 19(7):636, 2001.

[72] Peng Chen, Jiajun Gu, Eric Brandin, Young-Rok Kim, Qiao Wang, and Daniel Branton. Probing single dna molecule transport using fabricated nanopores.

Nano Letters, 4(11):2293–2298, 2004.

[73] Stijn Van Dorp, Ulrich F Keyser, Nynke H Dekker, Cees Dekker, and Serge G Lemay. Origin of the electrophoretic force on dna in solid-state nanopores. *Nature Physics*, 5(5):347, 2009.

[74] Grégory F Schneider, Stefan W Kowalczyk, Victor E Calado, Grégory Pandraud, Henny W Zandbergen, Lieven MK Vandersypen, and Cees Dekker. Dna translocation through graphene nanopores. *Nano Letters*, 10(8):3163–3167, 2010.

[75] Grégory F Schneider and Cees Dekker. Dna sequencing with nanopores. *Nature Biotechnology*, 30(4):326, 2012.

[76] Kyle Briggs, Harold Kwok, and Vincent Tabard-Cossa. Automated fabrication of 2-nm solid-state nanopores for nucleic acid analysis. *Small*, 10(10):2077–2086, 2014.

[77] Paolo Cadinu, Giulia Campolo, Sergii Pud, Wayne Yang, Joshua B Edel, Cees Dekker, and Aleksandar P Ivanov. Double barrel nanopores as a new tool for controlling single-molecule transport. *Nano Letters*, 18(4):2738–2745, 2018.

[78] Breton Hornblower, Amy Coombs, Richard D Whitaker, Anatoly Kolomeisky, Stephen J Picone, Amit Meller, and Mark Akeson. Single-molecule analysis of dna-protein complexes using nanopores. *Nature Methods*, 4(4):315, 2007.

[79] Stefan W Kowalczyk, Adam R Hall, and Cees Dekker. Detection of local protein structures along dna using solid-state nanopores. *Nano Letters*, 10(1):324–328, 2009.

[80] Benjamin N Miles, Aleksandar P Ivanov, Kerry A Wilson, Fatma Doğan, Deanpen Japrung, and Joshua B Edel. Single molecule sensing with solid-state nanopores: novel materials, methods, and applications. *Chemical Society Reviews*, 42(1):15–28, 2013.

[81] Sergii Pud, Daniel Verschueren, Nikola Vukovic, Calin Plesa, Magnus P Jonsson, and Cees Dekker. Self-aligned plasmonic nanopores by optically controlled dielectric breakdown. *Nano Letters*, 15(10):7112–7117, 2015.

Appendix

Fabrication Considerations

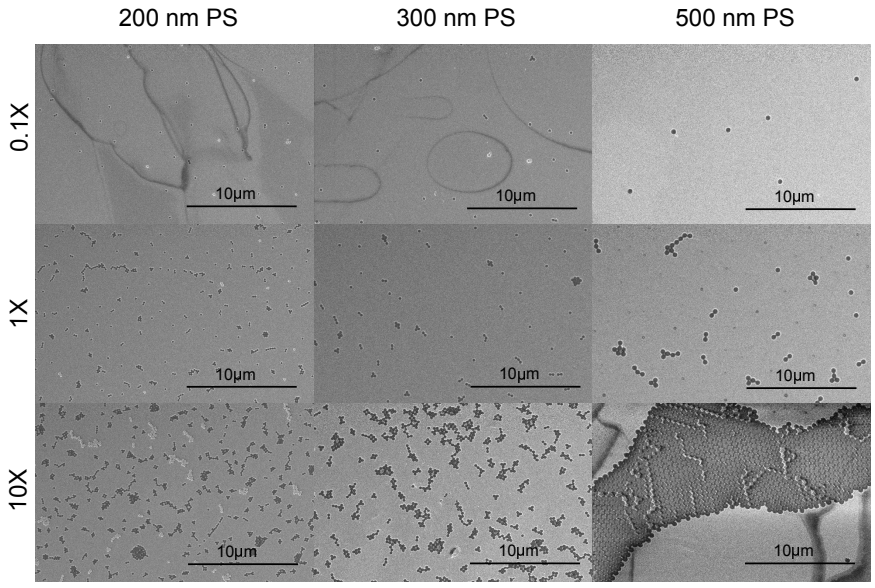

Figure A.1: SEM image matrix showing the apertures fabricated from colloidal lithography using 200 nm, 300 nm and 500 nm polystyrene spheres with varying concentrations.

Figure A.1 shows the SEM images of apertures fabricated using 200 nm, 300 nm and 500 nm polystyrene spheres with varying concentrations. A 1× concentration refers to a 0.01% w/v colloidal solution used in the fabrication process. Of the different concentrations used, 0.1× concentration results in predominantly single-nanoholes, whereas, the 10× concentration results in densely packed structures unsuitable for use in experiments.

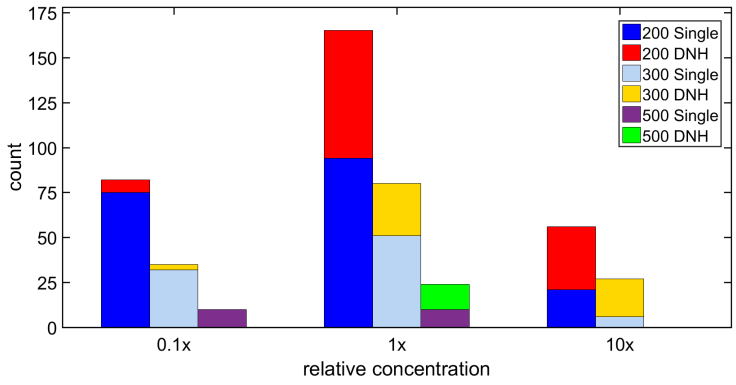

Figure A.2: A statistical distribution of double-nanoholes to single-nanoholes fabricated with colloidal lithography using 200 nm, 300 nm and 500 nm polystyrene spheres with varying concentrations.

The 1× concentration produced a favourable ratio of double-nanoholes to single-nanoholes of (76% from 200 nm, 56% from 300 nm and 140% from 500 nm) considering nine different samples. The distribution is shown in figure A.2.

Figure A.3 shows asymmetric apertures created after sonication when the sputter-coated gold layer has a thickness greater than the radius of the polystyrene spheres used in fabrication. After sonication, the nanospheres seem to rip through the surface, leaving behind undesired apertures.

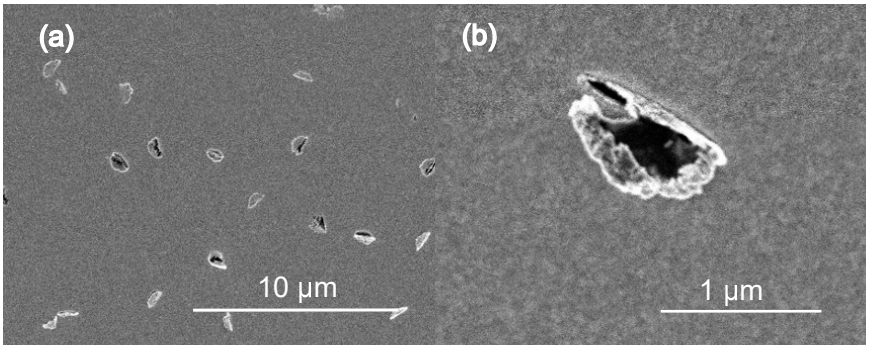

Figure A.3: Asymmetric rips created in gold when the sputtered layer thickness is greater than radius of polystyrene sphere.

Cross-talk

The diffraction limit of the optical trapping setup is approximately 1μm. The apertures fabricated for the experiment have nearest neighbours separated by a distance greater than the diffraction limit. This is ensured to prevent cross talk in measure-

ment from adjacent apertures. Generally, the double-nanoholes have a much larger separation between adjacent apertures than the single-nanoholes. From fabrication results, the double-nanoholes are typically 10 μm apart and hence avoid considerable cross-talk, even in the proximity of surface plasmon waves.

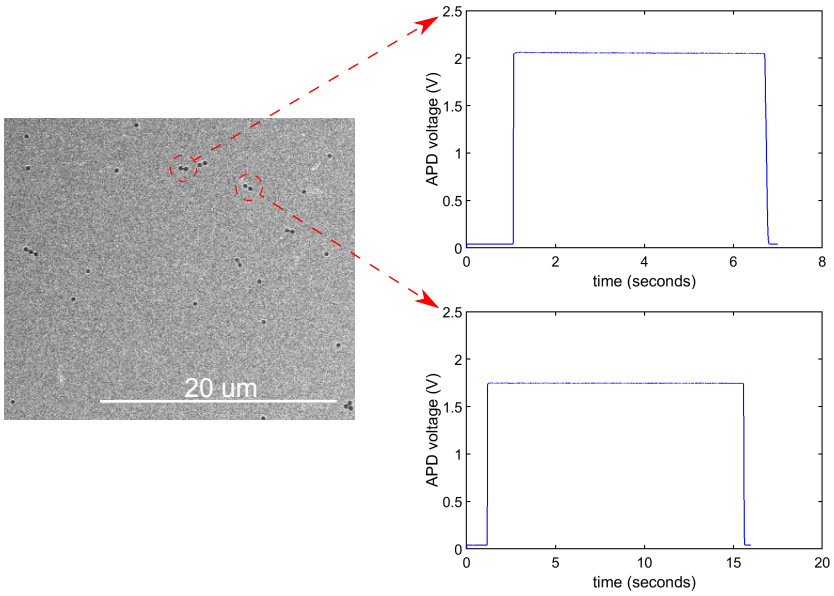

Figure A.4: Transmission measurement through double-nanoholes with cross-talk (top) and without (bottom) cross-talk.

Figure A.4 shows a small variation in transmission through double-nanohole apertures indicating cross-talk. In this case, two double-nanoholes close to one another (1 μm separation) give rise to cross-talk measuring 1.2$\times$ larger transmission than a typically isolated double-nanohole.

Malus' Law

The transmitted intensity of a linearly polarized light through a perfect polarizer is given by;

$$I = I_0 cos^2\theta, \tag{1}$$

where I_0 is the intensity of the incident light and θ is the angle between the axis of the polarizer and the incident polarized light. The degree of polarization is given by;

$$D = \frac{I_{\max} - I_{\min}}{I_{\max} + I_{\min}}. \tag{2}$$

I_{max} is the maximum transmitted intensity and I_{min} is the minimum transmitted intensity.

Optical Trapping Setup Alignment Guidelines

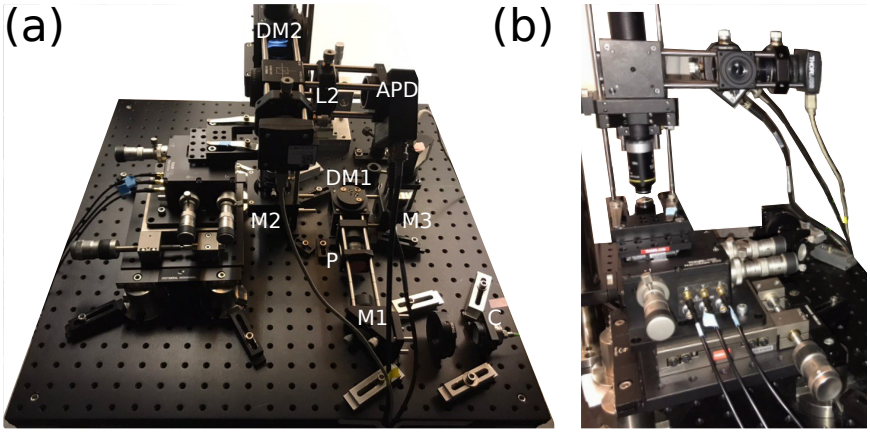

Figure A.5: (a) Top-view and (b) side-view of the modified optical trapping setup.

Figure A.5 shows the modified optical trapping setup used in carrying out the experiments detailed in this thesis. The following section provides guidelines for aligning the optical trapping setup. A detailed procedure on aligning the basic OTKB setup is provided in the equipment manual, available online on the Thorlabs website, and as a video on the Thorlabs YouTube channel.

Before commencing the alignment procedure, ensure that safety regulations are followed. Check if the laser controller is configured per the parameters provided in the laser diode specifications datasheet. Make sure all the connections in the setup are proper, fasten loose parts if any and tape down dangling fibers and wires. Make sure

the laser output from the collimator (C) is collimated. If not, perform collimation as specified in the component manual.

Next, measure the laser power after the linear polarizer using a power meter. Rotate the linear polarizer to obtain the maximum power measurable. The half-wave plate is critical during experiments to rotate the linearly polarized laser, from the linear polarizer, to align along the axis of the cusps of a double-nanohole aperture. This is to ensure maximum field confinement within the aperture and is favourable for trapping.

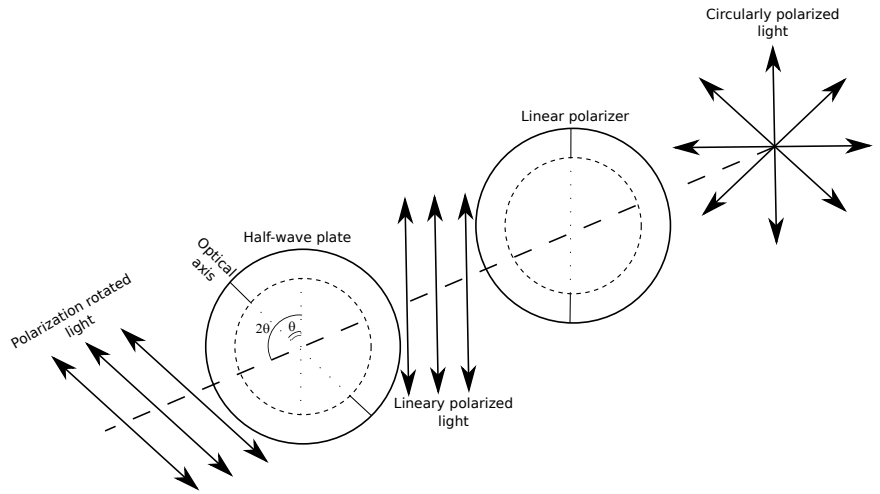

Figure A.6: Polarization limited output from a linear polarizer and rotation of linearly polarized light using a half-wave plate.

It is interesting to note that the half-wave plate is constructed from birefringent materials with different refractive indices along two orthogonal axes. The fast principal

axis of the half-wave plate has a lower refractive index. This results in the velocity for light polarized in this direction to be faster. Whereas, the slow axis of the half-ave plate has a higher refractive index. This results in the velocity for light along this polarization to be slower. A phase difference arises from the velocity difference between the two orthogonal polarization components . The angle between the output polarization and the input polarization is twice the angle between the input polarization and the wave plate's axis, as shown in figure A.6.

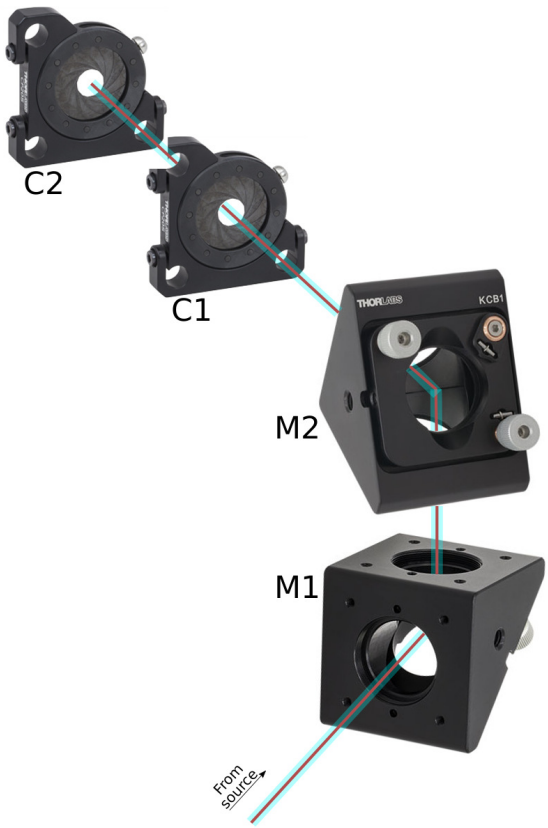

Figure A.7: Centering laser spot in an optical path.

While performing the alignment procedure, a line-walking method is adopted. This is depicted in figure A.7, where centering laser at a specific point in an optical path is achieved by adjusting the second closest controlling component. In the arrangement shown, mirror M1 is used to center the laser at C1 and mirror M2 to center the laser at C2. Multiple iterations might be necessary to align the beam properly. When commencing alignment on the optical trapping setup, an alignment plate with a visible alignment disk is used to locate the position of the laser at a point, P, between the mirror M1 and short-pass dichroic mirror DM1 in the beam expander path. Before proceeding, ensure that the dichroic mirror DM1 is mounted at 45°, without any tilt. Using the X–Y alignment screws on the collimator C, center the laser at P. Next, center the position of the laser on the alignment plate in front of mirror M2 by adjusting the screws on mirror M1.

In the vertical segment, make sure that the position of the microscope objectives mounts, with x–y translation, is such that the distance between the objectives when mounted is approximately a sum of their working distances (∼7.23 mm). Once this is ensured, remove the objectives and check for the position of the laser on the alignment plate at the collection objective mount. Center the location of the laser using M2. Next, ensure that the dichroic mirror DM2 is mounted at 45° without any tilt and center the laser in front of the APD using DM2. The lens L2 must be placed such that the APD sensor is at the focal point of the lens. Next, mount the objectives and

check for the center of the laser at a point after DM2. Use the x–y translation screws on the objective mounts to center the laser. Finally, measure the APD voltage on the DAQ DataLogger software and adjust the screws on the microscope objective mounts and the L2 lens mount for maximum reading. At this point, tweak the mirror M1 for very fine adjustments.

MATLAB Code

The optical trapping data is stored in a text log file by the Datalogger DAQ software. Figures for this data are generated using the MATLAB code below. Usually, a 101-point moving average filter window is used to reduce root-mean-square (RMS)-noise by a factor of 10. A Fourier analysis of the trapping data can also be performed using this code. The figures generated are later converted to an encapsulated postscript image format using Inkscape and uploaded to Overleaf for use in a manuscript.

Code:

```
close all;

clear all;

clc;


fid=fopen('Datalog_Filename.txt');
```

```
v=textscan(fid,'%.10f','headerlines',15);

fclose(fid);


y = v{1};


x = 1:length(y);

Ts = 1/100000;  %1/Sampling frequency


win =101;   %filter window

B = 1/win*ones(win,1);

out = filter(B,1,y);   %filtering to remove rms noise


x1 = 1:length(out);


baseline = mean(out(100000:200000)); %Normalizing untrapped state to 1


plot (x1*Ts,out/baseline);

title('Trapping');

grid on;

xlabel('time');

ylabel('normalized APD Voltage');
```

```
Fs = 100000;

L = length(y);


NFFT = 2^nextpow2(L);

z = fft(y,NFFT)/L;


f = Fs/2*linspace(0,1,NFFT/2+1);


figure (2)

plot(f,2*abs(z(1:NFFT/2+1)));

title('FFT analysis');

xlabel('frequency (Hz)');

ylabel('spectral magnitude');
```

***